



The cyclotron at the Ion Beam Laboratory ISL



Scientific highlights Structural Research 2004

BENSC User Service	36
ISL User Service	44
NAA User Service	48
SF1, Methods and Instruments	50
SF2, Magnetism	54
SF3, Materials	58
SF4, Structure and Dynamics	60
SF5, Theoretical Physics	66
SF6, Molecular Trace Element Research in the Life Sciences	70
SF7, Nuclear Measurements	72

Magnetisation plateaus in the quantum magnet NH_4CuCl_3

Ch. Rüegg^{1,2}, M. Oettli¹, J. Schefer¹, O. Zaharko¹, A. Furrer¹, H. Tanaka³, K.W. Krämer⁴, H.-U. Güdel⁴, P. Vorderwisch⁵, K. Habicht^{5,6}, T. Polinski⁵, M. Meissner⁶

■ 1 Laboratory for Neutron Scattering, ETH Zurich and Paul Scherrer Institute, Villigen PSI, Switzerland

■ 2 Department of Physics and Astronomy, University College London, UK ■ 3 Department of Physics, Tokyo

Institute of Technology, Japan ■ 4 Department of Chemistry and Biochemistry, University of Berne, Switzerland

■ 5 HMI, SF1 ■ 6 Institute of Solid State Physics, Technical University of Darmstadt, Germany

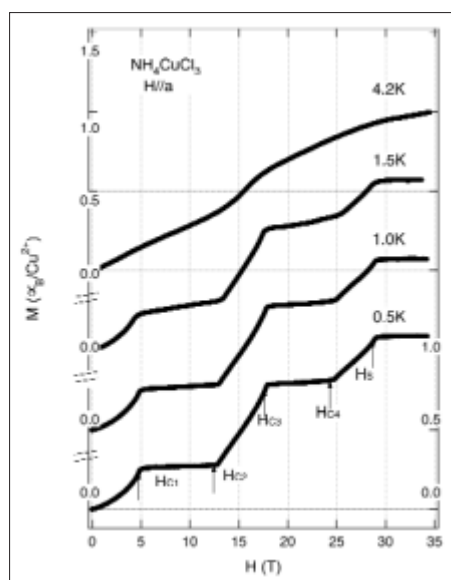


Fig. 1: Magnetisation curves of NH_4CuCl_3 measured at different temperatures with $H||a$, from Ref. [5]

a dominant antiferromagnetic exchange interaction. The resulting singlet state on each dimer is hereby protected by a spin energy gap from the magnetic triplet states as the elementary excitations. An external magnetic field can induce a quantum phase transition at the critical value H_c , where the onset of long-range magnetic order is observed [2, 3]. A related transition occurs also as a function of hydrostatic pressure [4]. However, the details of the uniform magnetisation are fundamentally different for $\text{SrCu}_2(\text{BO}_3)_2$ and TlCuCl_3 [1, 2]. The former shows distinct plateaus in this quantity at fractional values of the magnetic saturation ($m=1$) whereas the latter demonstrates the case of a uniform increase above H_c ($m=0$).

The ammonium substituted compound NH_4CuCl_3 was believed to be isostructural to TlCuCl_3 and therefore to show similar magnetic

properties. It therefore came as a surprise that the uniform magnetisation in NH_4CuCl_3 is characterised by magnetisation plateaus at $m=1/4$ and $m=3/4$, but on the other hand none at $m=0$, corresponding to a spin gap at $H < H_c$, see Fig. 1 [5]. The mystery in NH_4CuCl_3 and the mechanism leading to the plateau formation in general have consequentially been addressed by complementary experimental techniques including specific heat, NMR, and neutron scattering. The first plateau can fortunately be reached by the high-field equipment for neutron scattering at the Hahn-Meitner-Institut.

The investigations reveal the presence of several structural phase transitions leading to the space group P-1 at low temperatures with a doubling of the unit cell along the b -axis. The reduced symmetry in combination with the doubling of the unit cell defines three inequivalent dimer subsystems with volume fractions 25%, 50%, and 25%, see Fig.2 [6]. The segregation into different dimer subsystems is further reflected in the excitation spectrum measured by INS, which clearly identifies three modes in well-separated energy ranges, see

The investigations reveal the presence of several structural phase transitions leading to the space group P-1 at low temperatures with a doubling of the unit cell along the b -axis. The reduced symmetry in combination with the doubling of the unit cell defines three inequivalent dimer subsystems with volume fractions 25%, 50%, and 25%, see Fig.2 [6]. The segregation into different dimer subsystems is further reflected in the excitation spectrum measured by INS, which clearly identifies three modes in well-separated energy ranges, see

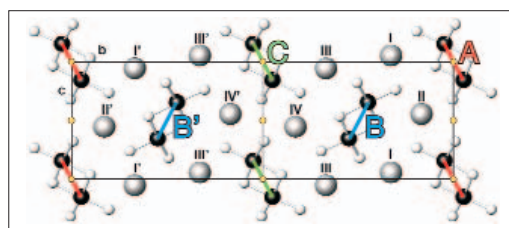


Fig. 2: Low-temperature structure of NH_4CuCl_3 in projection along the a -axis on the bc -plane. The high-temperature unit cell is doubled along the b -axis. Subsystems of Cu^{2+} dimers are marked by A, B, B' and C, inequivalent NH_4^+ groups by Roman numbers I-IV and I'-IV'. Orange circles denote inversion centres in case of space group P-1 where the primed sites become equivalent to the unprimed ones.

Fig.3 [6]. The absence of the $m=0$ plateau is explained by the gapless ground state resulting from the onset of long-range order, which is directly detected by antiferromagnetic Bragg peaks raising below $T=1.3$ K already in zero-field. The phase boundary has additionally been scanned by specific heat measurements performed at the Hahn-Meitner-Institut down to $T=0.3$ K and up to $H=6$ T. The field dependence of the excitation spectrum as measured by INS identifies successive quantum phase transitions of the dimer subsystems as the driving mechanism for the unconventional magnetisation process, in complete agreement with theoretical predictions [6, 7].

In NH_4CuCl_3 the first plateau sets in, when the subsystem A is completely polarised along the field direction. Accordingly the second plateau starts, when also the subsystem B reaches its complete saturation. The magnetisation rises at the edge of the first (second) plateau, when the individual spin gap of the dimer subsystem B (C) is closed and field-induced magnetic order occurs, similar to the soft-mode transition reported for TlCuCl_3 , see Fig.3 [3, 6, 7]. The energy splittings observed at $T=0.13$ K and $T=1.8$ K are identical, i.e. they are not affected by the onset of magnetic order. This directly proves that 75% (B and C) of the spin system remain in a gapped singlet state whereas 25% (A) order. The mode linearly increasing above H_{c1} is further interpreted as the field-induced opening of a spin gap for the subsystem A. This gap can be understood as the linear increase of the Zeeman energy for a triplet-singlet transition.

The investigation of quantum phase transitions in dimer spin systems demonstrates that especially the excitations characterise a ground state or its evolution as a function of an external parameter. The detection of long-range order is in the present context not conclusive in terms of a detailed statement about the ground-state wave function. To measure the excitation spectrum, in this case by INS, is therefore essential for a successful characterisation of the above transitions. The detected singlet-triplet condensate ground states in TlCuCl_3 and NH_4CuCl_3 are summarised in Fig. 4.

Triplet states are admixed to the singlet condensate in TlCuCl_3 above H_c . This occurs in a *homogeneous* way, i.e. each dimer site is involved due to the mobility of the triplet quasi-particles. In NH_4CuCl_3 the situation is more complex because of the three dimer subsystems, which are intimately related to the plateau formation. At $H_{c1} < H < H_{c2}$ inside the $m=1/4$ plateau, 25% of the dimers are in a field-aligned triplet state, whereas

75% are gapped. The singlet-triplet spin gap for the subsystem with 50% volume fraction is closed at H_{c2} . Accordingly, for $H_{c2} < H < H_{c3}$ triplet states are admixed on these dimers. The condensate in NH_4CuCl_3 is in this sense *inhomogeneous*. The generic case, found in $\text{SrCu}_2(\text{BO}_3)_2$, where the condensate is inhomogeneous without an explicit breaking of translational symmetry by a structural phase transition, could still occur in this field range in the layers of this 50%-subsystem. This possibility is not considered in Fig. 4 and was so far not observed experimentally.

The presented results about the field-induced phases in dimer spin systems are not limited to the investigated compounds. They are also valid for other dimer-based systems. The corresponding experiments on related materials have recently been performed or are planned for the near future.

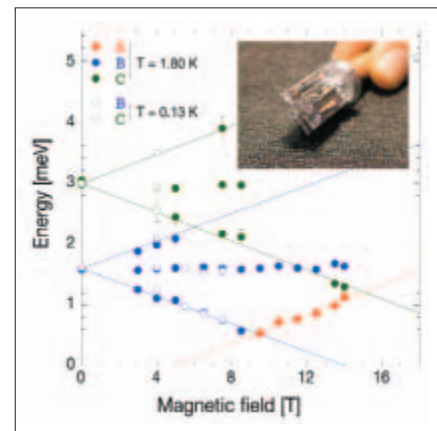


Fig. 3: Field dependence of the spin dynamics in NH_4CuCl_3 measured at $Q=(0\ 0\ 1)$, $T=1.8$ K and $T=0.13$ K. Inset: Six coaligned NH_4CuCl_3 single crystals on an Al sample holder. The individual crystals are wrapped into Al foil and glued at the top and bottom onto adjustable Al plates. The arrangement fits into Hahn-Meitner-Institut's 15-T cryomagnet for neutron scattering experiments.

- [1] T.M. Rice, *Science* **298**, 760 (2002)
- [2] K. Kodama *et al.*, *Science* **298**, 395 (2002)
- [3] Ch. Rüegg *et al.*, *Nature* **423**, 62 (2003)
- [4] Ch. Rüegg *et al.*, *Phys. Rev. Lett.* **93**, 257201 (2004)
- [5] W. Shiramura *et al.*, *J. Phys. Soc. Jpn.* **67**, 1548 (1998)
- [6] Ch. Rüegg *et al.*, *Phys. Rev. Lett.* **93**, 037207 (2004)
- [7] M. Matsumoto *et al.*, *Phys. Rev. B* **68**, 180403 (2003)

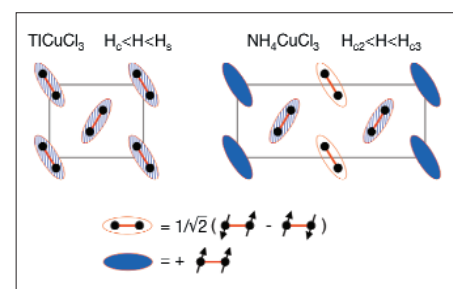


Fig. 4: Schematic representation of singlet-triplet condensates. Projection of a single unit cell along the a -axis on the bc -plane. Left: TlCuCl_3 above the critical field H_c but below saturation H_s . Right: NH_4CuCl_3 between the $m=1/4$ and $m=3/4$ plateau. 25% of the dimers are in the triplet state (field-aligned, dark blue). Light blue denotes triplet admixture.

Corresponding author:

C. Rüegg
c.ruegg@ucl.ac.uk

Does antiferromagnetism survive in the superconducting phase of CeCu_2Si_2 ?

O. Stockert¹, E. Faulhaber², K. Prokeš³, N. Stüßer³, S. Gerischer⁴, P. Smeibidl³, H.S. Jeevan¹, M. Deppe¹, C. Geibel¹, M. Loewenhaupt², F. Steglich¹

■ 1 Max-Planck-Institut für Chem. Physik fester Stoffe, Dresden, Germany ■ 2 Institut für Festkörperphysik, TU Dresden, Germany ■ 3 HMI, SF2 ■ 4 HMI, SF1

The interplay of superconductivity and antiferromagnetic order continues to be of general interest in condensed matter physics. While the coexistence of antiferromagnetism and superconductivity can easily be understood if different electronic subsystems are involved in the two phenomena, the situation might be different if the same electron system is responsible for both. In the case of the heavy-fermion compound CeCu_2Si_2 the Ce-4f electrons do not only order magnetically but are also involved in the formation of superconducting Cooper pairs. The strong electron correlations in CeCu_2Si_2 show up e. g. in a huge linear coefficient to the electronic specific heat at low temperatures, $\gamma = C/T \approx 1 \text{ J/molK}^2$, indicative of a largely enhanced effective electron mass. In consequence, such systems are called heavy-fermion systems [1].

growing technique improved quite a lot, now allowing to grow large single crystals with well defined properties. Recently, we could identify the antiferromagnetic order on a large A-phase single crystal by neutron diffraction [3]. Below $T_N \approx 800 \text{ mK}$ antiferromagnetic superstructure peaks have been detected and the ordered moment is estimated to $< 0.1 \mu_B$. The propagation vector τ of the magnetic A-phase order, $\tau = (0.215 \ 0.215 \ 0.530)$ at $T = 50 \text{ mK}$, appears to be determined by the nesting properties of the Fermi surface as indicated by renormalized band-structure calculations.

With the knowledge of the A-phase magnetism we started our investigation of the interplay between antiferromagnetism and superconductivity on an A/S single crystal with a $T_N \approx 700 \text{ mK}$ and a superconducting $T_c \approx 500 \text{ mK}$. We performed neutron diffraction experiments on the diffractometers E4 and E6 at temperatures below $T = 1 \text{ K}$ and in magnetic fields up to $B = 2 \text{ T}$. In order to address the question about the possible coexistence of superconductivity and magnetic order, it is of high importance to measure both phenomena simultaneously. Since neutrons are sensitive to antiferromagnetic order, but cannot directly probe superconductivity, we designed a setup to measure the bulk ac susceptibility in situ, i.e. during the neutron diffraction experiment. A small ac magnetic field is applied to the sample by an excitation coil and the susceptibility signal is measured by a pair of pickup coils. Excitation and pickup coils are made out of copper wire wound on a thin copper coil former to minimize absorption. The whole setup is displayed in Fig. 1a. The sensitivity to detect the superconducting transition is verified in temperature and field sweeps (cf. Figs. 1b and 3a).

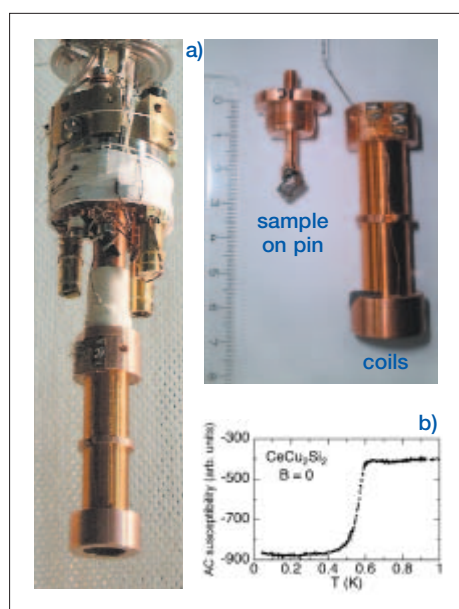


Fig. 1: a) Setup to measure the ac susceptibility on the neutron diffractometer. b) Temperature dependence of the ac susceptibility in CeCu_2Si_2 showing the onset of superconductivity at $T \approx 500 \text{ mK}$

The heavy-fermion compound CeCu_2Si_2 forms only in a very narrow range of the ternary phase diagram Ce:Cu:Si around the 1:2:2 composition. However, the ground state in CeCu_2Si_2 depends very delicately on the actual composition. Thus, Cu-rich samples exhibit only superconductivity and Si-rich only show a magnetically ordered phase called A-phase, while in stoichiometric samples (A/S-type) a complex interaction between superconductivity and magnetic order occurs [2]. During the last few years the crystal

Rocking scans across the positions of magnetic superstructure peaks were performed at different points in the magnetic (B, T) phase diagram as shown in Fig. 2a. Here, the (B, T) phase diagram is known from thermodynamic and transport measurements. We focused our study

to low temperatures and low magnetic fields in order to investigate the interplay between magnetic order and superconductivity. Our main results are displayed in Fig. 2b. In zero magnetic field just below the Neel temperature the magnetic Bragg peak is observed, but has disappeared at $T=400$ mK, i.e. well inside the superconducting phase. Applying at $T=400$ mK an overcritical magnetic field of $B=2$ T to kill superconductivity, leads to a recovery of the antiferromagnetic order. The absence of magnetic Bragg peaks in the superconducting phase gives evidence that in this crystal antiferromagnetism and superconductivity seem to exclude each other on a microscopic scale. These findings are in line with results obtained by μ SR and NMR measurements [4, 5]. A great advantage of the in situ susceptibility measurement is the possibility to perform measurements close to the phase boundaries. In particular, we investigated the transition from superconductivity to the A-phase at lowest temperature $T=50$ mK. From the bulk susceptibility the transition is at $B \approx 1.1$ T. Away from the phase boundary the results are as expected, i.e. no antiferromagnetic order in zero field and the recovery of antiferromagnetism at $B=2$ T. Surprisingly, at 1 T where the susceptibility indicates that the crystal is still superconducting, the magnetic Bragg peak is observed. We attribute this to the first-order nature of the phase boundary between superconductivity and antiferromagnetism which seems to be accompanied by phase separation. Experiments to clarify the situation in the vicinity of the phase boundaries will be continued in the near future.

In conclusion, we performed neutron diffraction with a newly developed in situ ac susceptibility setup and investigated an A/S-type CeCu_2Si_2 single crystal. Our measurements give evidence that superconductivity expels antiferromagnetism at low temperatures and that both phenomena do not coexist on a microscopic scale.

We greatly acknowledge the help of the whole sample environment team at BENSC. Without them, the experiment would not have been possible. Our work is supported by the Deutsche Forschungsgemeinschaft within Sonderforschungsbereich 463.

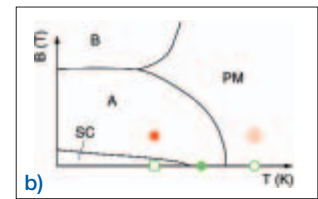
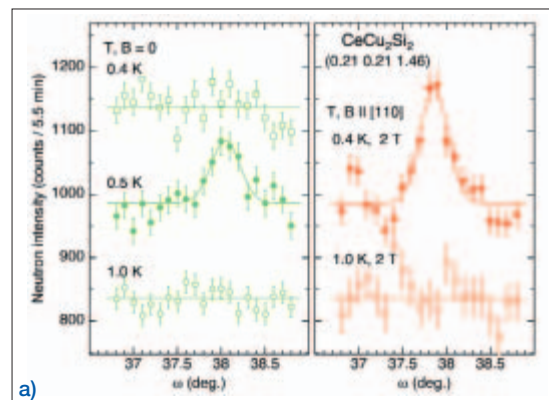


Fig. 2: **a)** Schematic magnetic (B, T) phase diagram of CeCu_2Si_2 with different magnetically ordered phases (A-, B-phase) and the superconducting phase. The (B, T) values at which

neutron diffraction measurements were performed, are marked. **b)** Rocking scans across the position of a magnetic superstructure peak in CeCu_2Si_2 at different temperatures and magnetic fields. While magnetic superstructure peaks are present in the A-phase, no magnetic peak has been detected in the superconducting phase. This indicates that superconductivity and antiferromagnetism exclude each other on a microscopic scale.

- [1] An introduction to heavy-fermion physics can be found e.g. in: N. Grewe, F. Steglich, *Handbook on the Physics and Chemistry of Rare Earths* (Elsevier Science Publishers B.V., Amsterdam, 1991), vol. 14, chap. *Heavy Fermions*, p. 343
- [2] F. Steglich *et al.*, *More is different – fifty years of condensed matter physics* (Princeton University Press, 2001), chap. 13, p. 191
- [3] O. Stockert *et al.*, Phys. Rev. Lett. **92**, 136401 (2004)
- [4] R. Feyerherm *et al.*, Phys. Rev. B **56**, 699 (1997)
- [5] K. Ishida *et al.*, Phys. Rev. Lett. **82**, 5353 (1999)

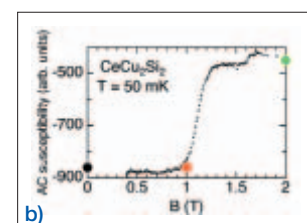
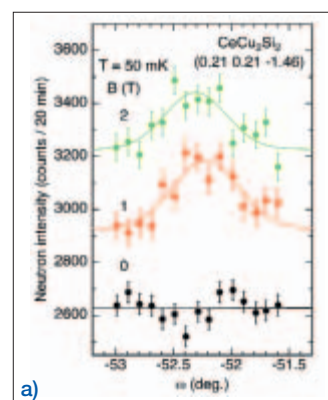


Fig. 3: **a)** Magnetic field dependence of the ac susceptibility at $T=50$ mK indicating the transition from superconductivity to the A-phase at $B \approx 1.1$ T.

b) Rocking scans as in Fig. 2 **b)** at $T=50$ mK for different magnetic fields (marked in **a)**). The existence of magnetic intensity at $B=1$ T points to a phase separation at the transition between A-phase and superconducting phase.

Corresponding author:
O. Stockert
stockert@cpfs.mpg.de

Tailoring surface coatings for protein immobilization

C. Czeslik¹, G. Jackler¹, R. Steitz²

■ 1 Universität Dortmund, Physikalische Chemie I, Dortmund, Germany ■ 2 HMI, SF1

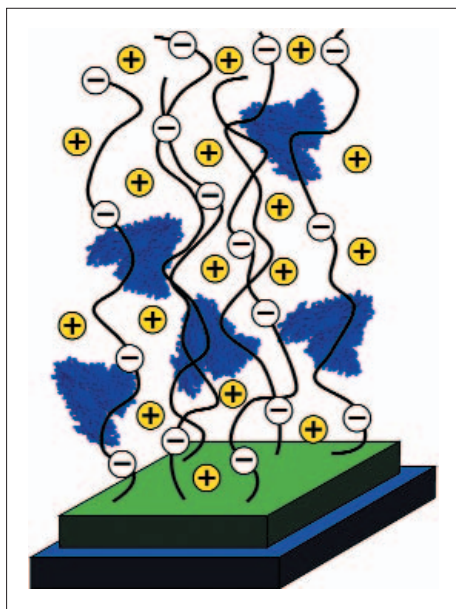


Fig. 1: Schematic drawing of a poly(acrylic acid) brush anchored on a thin poly(styrene) film that is deposited on a silicon wafer. The brush is characterized by a high concentration of trapped counterions. It can bind various amounts of protein depending on the ionic strength of the protein solution.

To vary the degree of protein adsorption at an interface, one may vary the pH-value or the ionic strength of the protein solution, in order to modify or shield the electric charge of the protein molecules and thus the electrostatic protein/interface interactions. However, a general variation of the degree of protein adsorption is principally not possible in this way. Thus, one has to develop functional surface coatings with a variable and controllable protein affinity.

As observed in numerous experimental studies, proteins adsorb spontaneously at almost all aqueous/solid interfaces [1, 2]. This phenomenon is also encountered in daily life, such as the adsorption of lysozyme onto contact lenses or the attachment of marine organism at ships using protein-based adhesives. There are also practical applications in which adsorbed proteins play a key role. For example, solid-phase immunoassays are used in medical diagnostics, such as pregnancy tests, where adsorbed protein antibodies bind antigens specifically.

In recent studies, the protein binding capacity of colloidal particles that are covered with a poly(acrylic acid) (PAA) brush has been determined [3, 4]. It has been found that these PAA brush particles bind huge amounts of proteins at low ionic strength and neutral pH-values where the PAA is dissociated and negatively charged. Interestingly, when the ionic strength of the solution is increased to a few 100 mmol/L, the PAA brush particles appear essentially protein resistant regardless of the protein net charge. Thus, by varying the ionic strength of the solution over a relatively small range, the protein affinity of the PAA brush particles can be switched between high and low. It is noted that this effect is not related to a simple electrostatic screening, since the effect has also been observed for the protein BSA that binds to the PAA brush particles under electrostatic repulsion.

Using neutron reflectometry the protein binding capacity of a planar PAA brush has been studied for the first time (Fig. 1) [5]. The planar PAA brush has been prepared by spin-coating a thin poly(styrene) film onto a silicon wafer. Then, the diblock copolymer poly(styrene)-poly(acrylic acid) was transferred to the modified Si wafer applying the Langmuir-Schäfer technique.

In Fig. 2, selected neutron reflectivity curves are shown which were obtained when the planar PAA brush was in contact with a pure buffer solution, a buffer solution containing BSA, and a buffer solution containing BSA and 500 mmol/L sodium chloride. From a simple visual inspection of the three curves, one may conclude that in the presence of sodium chloride the planar PAA brush appears to be protein resistant, since the corresponding reflectivity curve essentially overlaps with that of the pure buffer solution. This overlap indicates an unchanged interfacial structure. In contrast, without added salt, BSA binds to the planar PAA brush under electrostatic repulsion, since the reflectivity curve of the pure buffer solution is changing significantly upon adding BSA to the solution. Thus, a functional surface coating has been generated which can be used to switch the protein affinity of an interface.

A detailed analysis of all the measured neutron reflectivity curves indicates that BSA is penetrating deeply into the planar PAA during adsorption at low ionic strength (Fig. 3). Since BSA and PAA are like-charged and no adsorption takes place at elevated ionic strength, BSA must be immobilized at the planar PAA brush by a driving force different from ionic, van der Waals and hydrophobic interactions.

Indeed, a simple mean field model has been developed that predicts a large gain of free energy due to a release of BSA counterions on transferring a BSA molecule from the solution into a PAA brush [5]. The free energy of this counterion *evaporation* is entropic in nature and dominates over the direct electrostatic repulsion between the protein and the like-charged brush. The reason for this loss of ions is the enormous excess of positively charged counterions in the PAA brush requiring a lower number of BSA counterions only. As the ionic strength of the protein solution is raised, this counterion release force is vanishing rendering a PAA brush protein resistant.

The experimental and theoretical results of this study therefore suggest a new fundamental driving force for protein adsorption at interfaces. Since a change of the ionic strength over a few 100 mmol/L mainly leaves the structure and dynamics of dissolved protein molecules unaffected, the switching of the protein affinity of a PAA brush by changing the ionic strength of the protein solution is likely to be protein independent, and its use in biotechnological applications appears to be rewarding.

-
- [1] M. Malmsten (ed.), *Biopolymers at interfaces*, Marcel Dekker, New York (2003)
 [2] C. Czeslik, *Z. Phys. Chem.* **218**, 771 (2004)
 [3] A. Wittemann, B. Haupt, M. Ballauff, *Phys. Chem. Chem. Phys.* **5**, 1671 (2003)
 [4] C. Czeslik, R. Jansen, M. Ballauff, A. Wittemann, C.A. Royer, E. Gratton, T. Hazlett, *Phys. Rev. E* **69**, 021401 (2004)
 [5] C. Czeslik, G. Jackler, R. Steitz, H.-H. von Grünberg, *J. Phys. Chem. B* **108**, 13395 (2004)

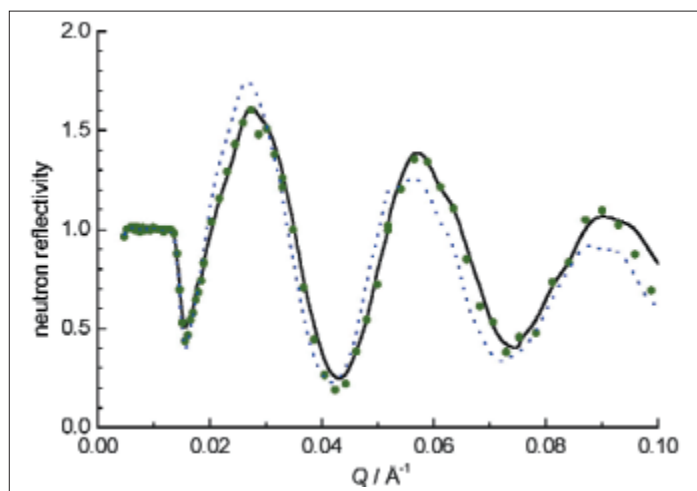


Fig. 2: Neutron reflectivity curves of a silicon/solution interface that has been modified with a planar PAA brush (see Fig. 1). The curves are normalized to that of a smooth Si/water interface. Data are shown for a pure buffer solution (black solid line), a buffer solution containing the protein BSA and NaCl (green symbols), and a buffer solution containing BSA without NaCl (blue dotted line). The data indicate BSA binding to the PAA brush in the absence of NaCl only which can be explained by a release of counterions.

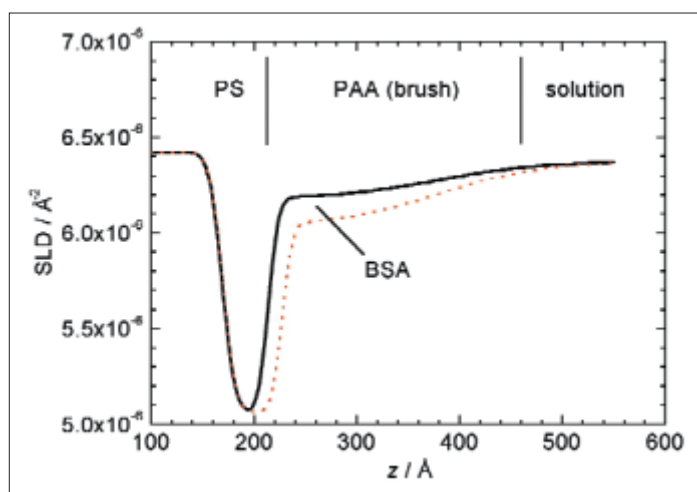


Fig. 3: Scattering length density (SLD) profile of a planar PAA brush (see Fig. 1) with and without immobilized protein (BSA). The difference between the two profiles is proportional to the protein volume fraction.

Corresponding author:

C. Czeslik
 claus.czeslik@uni-dortmund.de

Structural explanation of the magneto-electric phase transitions in HoMnO_3

Th. Lonkai^{1,2}, U. Amann^{1,3}, J. Ihringer¹, D. Hohlwein^{1,2}, Th. Lottermoser⁴, M. Fiebig⁴

■ 1 Institut für Angewandte Physik, Universität Tübingen, Germany ■ 2 HMI, SF2 ■ 3 Institut Laue-Langevin, Grenoble, France ■ 4 Max-Born-Institut, Berlin, Germany

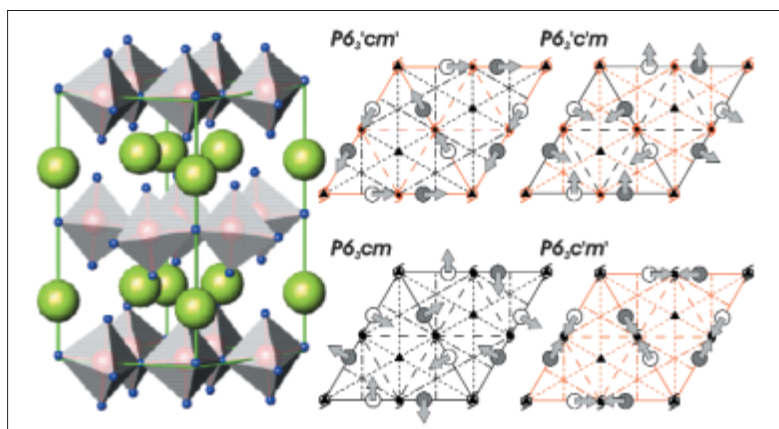


Fig. 1: Nuclear and magnetic structure of HoMnO_3 . The hexagonal manganite HoMnO_3 is formed of planes of corner connected tilted and distorted MnO_5 -coordination polyhedra, separated by corrugated R -planes, Mn red, O blue, Ho green. The magnetic space groups are depicted on the right light (dark) spheres are Mn atoms with $c=0$ ($c=1/2$).

As the data density in conventional information storage reaches its physical limits, alternative concepts are analysed. The linear magneto-electric effect, i.e. the induction of a magnetic polarization due to an electric field and vice versa, provides a possibility to manipulate magnetic data by other means than magnetic fields. In HoMnO_3 single crystals with electric field of $E \sim 10^5 \text{ V/cm}$, we evidenced the control of the magnetic ordering by magneto-optical methods, the magnetic ordering is switched from antiferromagnetic to ferromagnetic. By neutron and x-ray powder diffraction, we derived an explanation of the magneto-electric phase transitions.

In zero field hexagonal HoMnO_3 traverses the magnetic phases $P6_3c'm$, $P6_3c'm'$, and $P6_3cm$, the phase transitions are at $T_N \sim 70 \text{ K}$, $T_R \sim 40 \text{ K}$, and

$T_{\text{Ho}} \sim 5 \text{ K}$, respectively [1, 2]. With an electric field of 10^5 V/cm , a different magnetic space group, $P6_3c'm'$ is formed below Néel-temperature (see Fig. 1). This was evidenced by magneto-optical methods (second harmonic generation and Faraday rotation [3].)

For a deeper understanding of this dramatic change in the magnetic structure of HoMnO_3 due to electric fields, a detailed understanding of the structure is essential. The electric ordering process was explained recently by group-theoretical methods and confirmed by neutron and x-ray powder diffraction. Hexagonal manganites traverse through two structural phase transitions at $T_{\text{npt}} \sim 1300 \text{ K}$ and $T_{\text{FE}} \sim 1000 \text{ K}$, from the paraelectric high temperature phase $P6_3/mmc$ to the ferroelectric low temperature phase, Fig. 2. In the high temperature phase, $T > T_{\text{npt}}$, the MnO_5 coordination polyhedra are undistorted with an O-Mn-O axis parallel c , while the R -planes, separating the planes of the

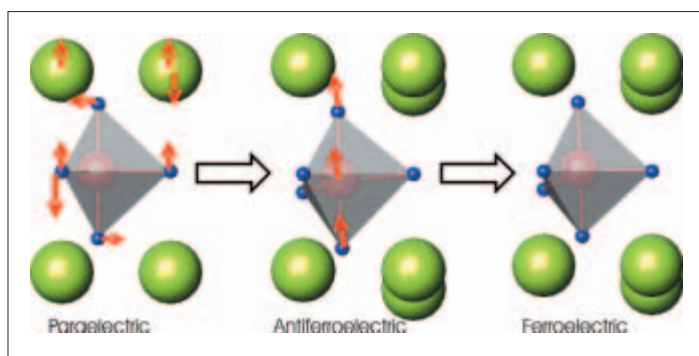


Fig. 2: Electric ordering process in HoMnO_3 in detail. In the paraelectric high temperature phase of the symmetry $P6_3/mmc$ the coordination polyhedra are straight and undistorted. In a first phase transition at $T_{\text{npt}} \sim 1300 \text{ K}$, the coordination polyhedra tilt and are distorted, while the Ho-planes become corrugated. The space group $P6_3cm$ is formed and an antiferroelectric phase is generated. Finally, at $T \sim 1000 \text{ K}$, a displacement of the O-Mn-O axis within the MnO_5 coordination polyhedra triggers a second phase transition, without a further change of symmetry, the ferroelectric low temperature phase is formed.

corner connected MnO_5 are flat – the structure is paraelectric. In a first phase transition at $T=T_{\text{npt}}$ the coordination polyhedra tilt and the R -planes become corrugated. Though the structure obeys the ferroelectric space group $P6_3cm$, it is still antiferromagnetic, until, in a second phase transition at $T=T_{\text{FE}}$ the O-Mn-O axis within the coordination polyhedra is displaced and a spontaneous electric polarization appears [4].

With a careful analysis of the results of Rietveld refinements of neutron and x-ray powder data (E2 [5], Hahn-Meitner-Institut, Berlin and high resolving Guinier diffractometer [6] with image plate [7], Tübingen [5]) of HoMnO_3 -powdered samples the magnetoelectric phase transitions can be explained. At lower temperatures, $T < T_{\text{Ho}} \sim 5$ K, the onset of Ho-ordering induces a magnetic phase transition from $P6_3c'm'$ to $P6_3cm$, and by this, a displacement of the O-Mn-O axis. Thus, the inter-planar magnetic exchange paths are changed, and by this, the electric polarization of the unit cell, Fig. 3. At higher temperatures with applied electric field, an equivalent process is induced. The electric field displaces the O-Mn-O axis of the MnO_5 coordination polyhedra, thus the magnetic exchange paths are changed and for the inter-planar coupling, a δ_3 -axis instead of a δ_3' -axis becomes favourable. The ferromagnetic space group, $P6_3c'm'$, which is formed now, requires a ferromagnetic ordering of the Ho moments parallel c , Fig. 4. In this space group, the magnetoelectric term lowers the overall energy of the system.

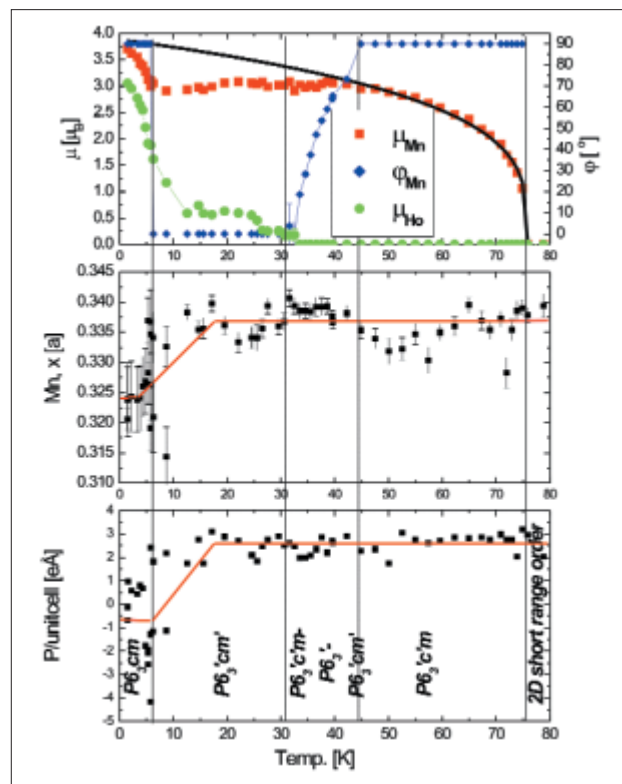


Fig. 3: Intra planar antiferromagnetic Ho ordering contradicts the symmetry $P6_3c'm'$, a new symmetry $P6_3cm$ is formed. The different coupling between the planes, δ_3 -axis instead of δ_3' -axis, requires different magnetic exchange paths, this leads to a change in the electric polarization: The O-Mn-O axis of the coordination polyhedra is shifted.

- [1] Th. Lonkai, D. Hohlwein, J. Ihringer, W. Prandl, Appl. Phys. A **74**, S843–S845 (2002)
- [2] M. Fiebig, C. Degenhardt, R.V. Pisarev, J. Appl. Phys. **91**(10), 8867–8869 (2002)
- [3] Th. Lottermoser, Th. Lonkai, U. Amann, D. Hohlwein, J. Ihringer, M. Fiebig, Nature **430**, 541–544 (2004)
- [4] Th. Lonkai, D.G. Tomuta, U. Amann, J. Ihringer, D. Toebbens, R. Hendriks, J. Mydosh, Phys. Rev. B **69**, 134108 (2004)
- [5] <http://www.hmi.de/bensc/misc/flat-cone/index.html>
- [6] <http://www.uni-tuebingen.de/uni/pki/guinier/guinier.html>
- [7] <http://www.uni-tuebingen.de/uni/pki/guinier/bildplatte.html>

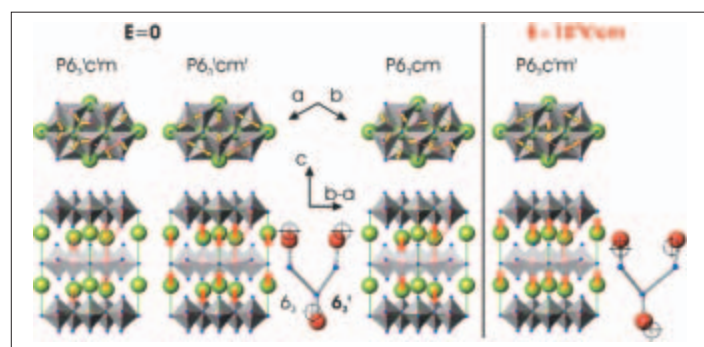


Fig. 4: The influence of the displacement of the O-Mn-O axis to the inter-planar magnetic exchange paths and structural explanation of the magnetoelectric phase transitions in HoMnO_3 . Due to the displacement of the O-Mn-O axis within the MnO_5 coordination polyhedra in an applied electric field, the inter-planar magnetic exchange paths are changed. A δ_3 -axis as inter-planar coupling becomes more favourable than a δ_3' -axis. The magnetic symmetry $P6_3c'm'$ is formed, which allows a magnetoelectric term, that leads to a lowering of the overall energy of the system.

Corresponding author:

T. Lonkai
thomas@lonkaimayer.de

Nanoscale self-assembly of thin oxide films under swift heavy ion bombardment

W. Bolse, A. Feyh, D. Etissa-Debissa, M. Kalafat

■ Institut für Strahlenphysik, Universität Stuttgart, Germany

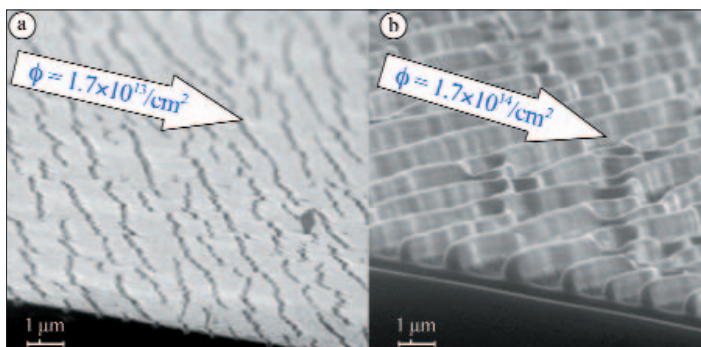


Fig. 1: Development of a 130 nm NiO/SiO₂ film during irradiation with 230 MeV Xe at a tilt angle of 75°. The arrows indicate the projection of the beam direction onto the sample surface.

During the last years, beams of swift heavy ions (SHI) of some MeV/amu have established themselves as excellent tools for nano-structuring of thin films and surfaces. A heavy ion of this kind deposits a huge amount of its kinetic energy almost instantaneously into a highly localized volume of nm-dimensions (at least laterally). The average energy deposited per atom may significantly exceed the binding energy of the solid and thus result in a nano-scale zone of extreme conditions (high temperature and pressure). The energy dissipation into the cold surrounding occurs within some tens of picoseconds and leads to rapid solidification of the excited track. This highly localized process (in space and in time)

can be regarded as a transient melting and rapid quenching mechanism, which drives the solid far from equilibrium and often leaves behind a nm-wide track of non-equilibrium material (for example the often observed amorphous tracks in insulators). Such extremely short and intense solid

state excitations, localized in a nano-scale volume, cannot be achieved by any other technique for material modification, and hence, single energetic ions offer a unique method to generate non-equilibrium phases with novel structural and physical properties and nm-dimensions. However, in recent years (and especially due to the intense and stable high energy ion beam provided by Hahn-Meitner-Institut's Ion Beam Laboratory – the Ionenstrahllabor ISL) it was discovered that not only single ion impact can be used to generate spatially separated nanoscale structures, but in many cases the application of high ion fluences may result in structural instabilities and a corresponding, often periodic, nanoscale patterning of surfaces and thin films. The properties of such self-organized structures usually surpass by far a simple superposition of the single-ion effects.

We have recently investigated the nano-scale self-assembly of thin Nickel-Oxide films triggered by SHI irradiation under inclined ion incidence [1–4]. Fig. 1 shows the scanning electron microscopy (SEM) images of a 130 nm thick NiO film on SiO₂ after irradiation with 230 MeV Xe-ions at fluences of $1.7 \times 10^{13}/\text{cm}^2$ and $1.7 \times 10^{14}/\text{cm}^2$. The sample was tilted by 75° with respect to the beam direction and kept at a temperature of 80 K. The arrows indicate the projection of the beam direction onto the surface. At low fluences, the surfaces exhibit an almost periodic crack pattern with typical distances of the order of 1 μm and oriented perpendicular to the beam direction. According to Trinkaus [5], the transient melting in the ion track generates tensile stresses along the track axis, which at grazing ion incidence results in an almost uni-axial in-plane stress field along the beam direction. As soon as these stresses exceed the critical fracture stress of NiO, the film becomes unstable (Grinfeld-instability [6]) and a periodic crack pattern forms. Further irradiation then results in shrinking of the material between the cracks and a growth in height due to the *hammering effect* [7]. Finally, a periodic lamellae-like structure is formed. The average height and distance of the *nano-walls* is of the order of 1 μm and their thickness is about 100 nm. These quantities strongly depend on the

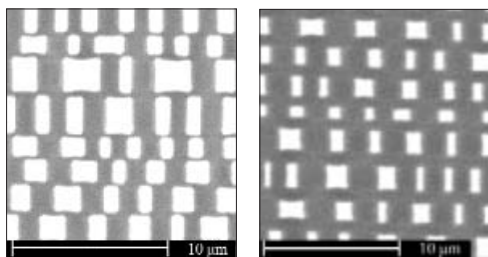


Fig. 2: a) 60 nm NiO/SiO₂ after double irradiation with 230 MeV Xe-ions (90° azimuthal rotation, $10^{14}/\text{cm}^2$ each direction, tilt angle 85°) b) same sample after additional irradiation under continuous azimuthal rotation (230 MeV Xe, 85°, $3 \times 10^{14}/\text{cm}^2$)

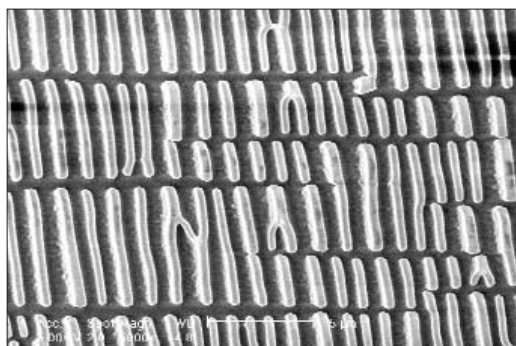


Fig. 3: Combination of Ar- and Au-irradiation, 90 nm NiO/SiO₂: stick-like structure

electronic stopping power of the ion and the initial film thickness, which on the other hand can be used to custom tailor the structural parameters. The disorder of the structure (cross-links between the lamellae) increases with increasing ion mass and decreases with increasing tilt angle and NiO thickness. Electron- and ion-microbeam analysis revealed that the initially coherent and smooth NiO-layer has quantitatively transformed into the lamellae-structure. No NiO is left on the substrate surface in between the walls.

Our knowledge of this self-assembly process, its underlying mechanisms and the way it depends on the irradiation conditions allowed us to produce more complex and custom tailored nanostructures by multiple irradiation of the sample under different azimuthal angles or even continuous rotation. Additional irradiation after an azimuthal rotation of the target by 90° again induces cracking and shrinking of the material, perpendicular to the already existing cracks. That way, rectangular structures evolve as shown in Fig. 2. With a combination of a light and a heavy ion-species in the subsequent irradiations, more

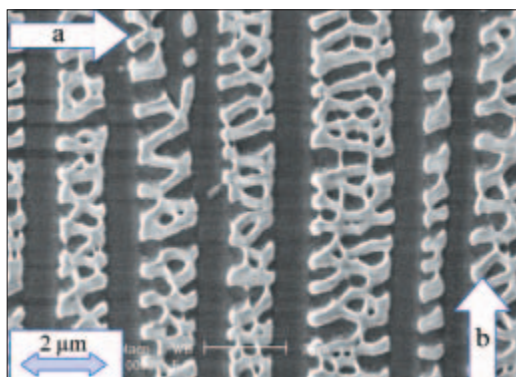


Fig. 4: Combination of Ar- and Au-irradiation, 40 nm NiO/SiO₂: nano-script

elongated structures are achieved (Fig. 3). When very thin NiO films are used, very complex patterns – like the *nano-script* shown in Fig. 4 – can be generated.

If one irradiates an existing structure at grazing SHI-incidence and under continuous azimuthal sample rotation, one can achieve an almost uniform reduction of its lateral dimensions, as is demonstrated in Fig. 2b. Consequently we have tried, instead of producing quadratic pillars by double-irradiation, to use multiple irradiations (0°, 90°, 135°, 225°, ...) and generate polygon-like structures. By finally irradiating these under continuous azimuthal rotation, we wanted to arrive at circular cylinders with diameters as small as possible. The result can be seen in Fig. 5, which shows a perspective view of a sample treated as described before. In fact, we were able to produce NiO *nano-towers* with a diameter of about 200 nm and a height of about 2 μm. The alignment of the *nano-towers* is rather regular, reflecting the periodicity of the crack formation described above. The towers cover only about 5% of the substrate surface. Since the wavelengths of the cracks depend on the film thickness the number density of the *nano-towers* decreases exponentially with the initial NiO thickness.

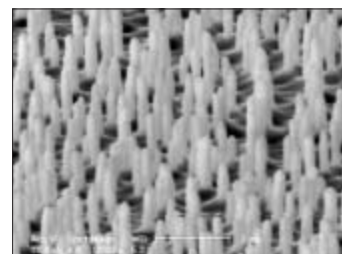


Fig. 5: Perspective SEM image of a NiO/SiO₂ sample after multiple single-step irradiations and subsequent continuous rotation irradiation. For details see text.

In conclusion we have demonstrated the very impressive potential of SHI to generate large-area covering nano-structures by initiating surface instabilities and self-assembly processes. The structures can be very much custom-tailored by choosing proper irradiation conditions.

- [1] W. Bolse, B. Schattat, A. Feyh, *Appl. Phys. A* **77**, 11 (2003)
- [2] A. Feyh, diploma thesis, Stuttgart University (2002)
- [3] D. Etissa-Debissa, master thesis, Stuttgart University (2003)
- [4] M. Kalafat, diploma thesis, Stuttgart University (2002)
- [5] H. Trinkaus, A.I. Ryazanov, *Phys. Rev. Lett.* **74**, 5072 (1995)
- [6] M.A. Grinfeld, *Dokl. Akad. Nauk. SSSR* **290**, 1358 (1986), D.J. Srolovitz, *Acta Metall.* **37**, 621 (1989)
- [7] S. Klaumünzer, G. Schumacher, *Phys. Rev. Lett.* **51**, 1987 (1983)

Corresponding author:

W. Bolse
bolse@ifs.physik.uni-stuttgart.de

10 years of materials analysis with heavy ions at ISL

W. Bohne, J. Röhrich, E. Strub

■ HMI, SF4

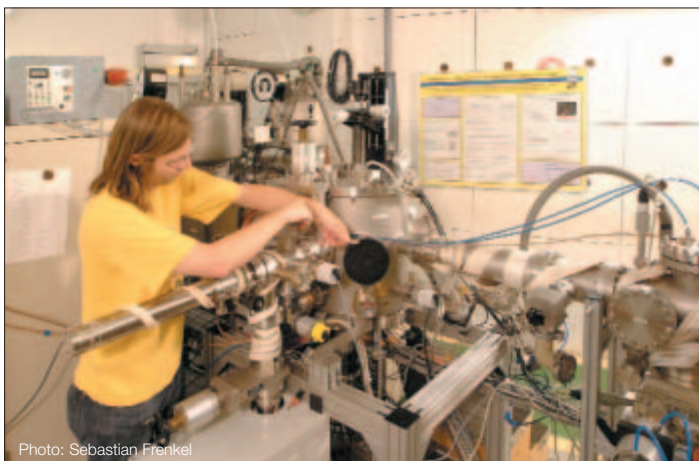


Photo: Sebastian Frenkel

Fig. 1: The time-of-flight ERDA set up

After finishing the nuclear physics research activities at VICKSI in the early nineties we started to use the modified accelerators as tools for materials characterisation. At first in 1994, a relatively simple set up was installed at the low energy beam line TR of the Van-de-Graaff accelerator to perform HI-RBS (Heavy Ion Rutherford Backscattering Spectroscopy) measurements. With 15 MeV N ions as projectiles and a detector system with a large solid angle of 22 msr a good detection sensitivity as low as 10 ppm for heavy elements in light matrices and a much better mass resolution compared to standard RBS with He beams was achieved. But, due to the dependence of the Rutherford cross section on mass and on the atomic number of the sample atom, the sensitivity decreases to only about 0.1% for light elements. And elements lighter than Ne are not detectable at all. To overcome these restrictions and drawbacks we decided to implement the ERDA method (Elastic Recoil Detection Analysis) which will be described a bit more in detail in the next paragraph.

ERDA is the complementary part of the RBS. Instead of detecting at backward angles the elastically scattered projectiles the corresponding recoiling ions of the sample constituents are measured. The situation is more complica-

ted because we are not dealing with the well known mass of the projectiles but with the normally unknown elements from the sample. That implies that in addition to the energy the mass of the recoils must be determined, that is, an energy and mass dispersive spectrometer becomes necessary. So for all contributing elements the corresponding energy spectra yield the same information as an RBS spectrum but now separately for each element. The intensity gives the atomic concentration and from the measured energy the depth where the scattering happened can be calculated. In contrast to RBS, **all** chemical elements can be detected simultaneously and the Rutherford cross section in the frame of the recoils is almost constant for all elements and even by a factor of four enhanced in the case of hydrogen, i. e., all elements are detectable with the same sensitivity. Like for RBS, the basic process for ERDA is the elastic Rutherford scattering for which the cross section can be calculated exactly. Therefore, ERDA is an absolute and quantitative method which does not need standard samples. All these advantages make ERDA a very valuable method to analyse complicated new materials.

To implement this nice technique, we designed in parallel to the operation of RBS a set up for ERDA. Owing to our experiences from nuclear physics experiments, we decided to make use of the time-of-flight (TOF) method for the mass

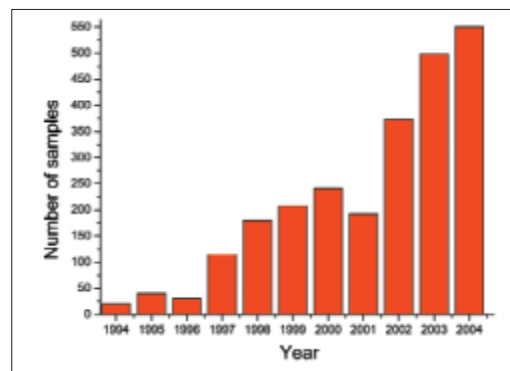


Fig. 2: Number of analysed samples per year

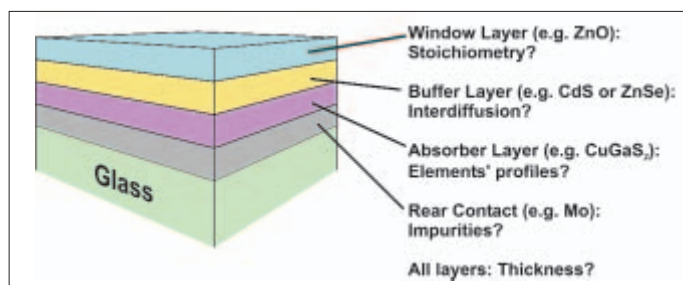


Fig. 3: Sketch of a thin film solar cell and typical questions that can be answered by ERDA

identification, because this technique offers the best dynamic energy range concerning mass separation, i. e., analysable depth. When simultaneously measuring the energy E and the corresponding velocity v via the flight time of each recoil and displaying this data in a two-dimensional spectrum, the *scatter plot*, all events of a certain mass M are grouped on one curve according to the relation $E = 1/2 Mv^2$. After disassembling the nuclear physics experimental set up, the spectrometer was realised at the high energy beam line TC. Figure 1 shows the present status. With this set up a detection sensitivity for all elements of about 10 ppm and a depth resolution in the 10 to 50 nm region, depending on depth, can be achieved. Films with a thickness of a few mono-layers up to some microns become analysable. A detailed description is given in [1]. Already in summer 1996 the first experiments had been performed. After presenting the first results, many materials scientists took stock in this method and the amount of samples we analysed grew steadily as demonstrated by Fig. 2.

Since the late nineties the new materials for the construction of thin film solar cells are a main focus of the ERDA studies. A fruitful collaboration between the ion-beam analysis and many groups from the solar-energy department at the Hahn-Meitner-Institut has developed, now using about 60% of the ERDA beam time. A thin film solar cell consists of several layers on a substrate as schematically depicted in Fig. 3. Especially in the case of the chalcopyrite cells, different physical and chemical deposition methods are implemented for the absorber, for the buffer, and for the TCO-window layer as well, resulting in various problems concerning contamination, stoichiometry, homogeneity, etc. By ERDA measurements many of these questions for certain layers and complete stacks have been answered, often allowing an improvement of the deposition process and of the quality of the cells. As an exam-

ple Fig. 4 shows the scatterplot obtained with 350 MeV Au ions as projectiles from a heterojunction consisting of a ZnSe buffer on a Cu(In,Ga)(S,Se)₂ absorber with a Mo back contact deposited on glass. The apprehension was that at higher temperatures used for the chemical vapour deposition (CVD) of the ZnSe an interdiffusion of elements of the absorber and buffer may happen. And indeed, at process temperatures above 350°C the diffusion of In into the buffer was observed [2, 3]. By the way, the iodine used as transport medium for the CVD can be clearly seen as a contamination in the ZnSe film. The inset, showing the surface region, demonstrates that due to the good mass resolution a separation of the overlapping Cu and Zn is possible with the aid of the well isolated ⁶⁸Zn isotope.

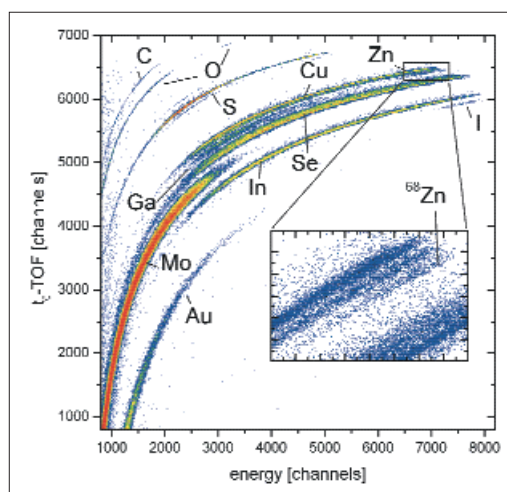


Fig. 4: Time-of-flight vs. energy spectrum for a heterostructure Cu(In,Ga)(S,Se)₂/ZnSe (~1000/70 nm thick) on Mo covered glass measured at 40° with a beam of 350 MeV Au. The inset shows in detail the Cu/Zn interface region.

- [1] W. Bohne, J. Röhrich, G. Röscher, Nucl. Instrum. and Meth. B **136–138**, 633 (1998)
- [2] W. Bohne, S. Lindner, J. Röhrich, Nucl. Instrum. and Meth. B **188**, 1–4, 55 (2002)
- [3] S. Lindner, W. Bohne, A. Jäger-Waldau, M. Ch. Lux-Steiner, J. Röhrich, G. Vogl, Thin Solid Films **403–404**, 432 (2002)

Corresponding author:

W. Bohne
bohne@hmi.de

Investigation of heavy metal release during thermal waste treatment on a forward-acting grate using radiotracers irradiated at BER II

T. Jentsch¹, D. Alber²

■ 1 Fraunhofer Institute for Nondestructive Testing, Branch Lab Dresden, Germany ■ 2 HMI, SF6

The possibilities for optimizing the process control in the so-called classical combustion of residual waste in grate systems have not yet been completely explored. One of the main objectives of the optimization is the improvement of the ash quality. The immediate goal of these investigations is the production of an ash that can be implemented in the construction industry with the condition that the necessary quality is achieved by primary measures, i.e. the process control itself, only. A prerequisite for this is the maintenance or reduction of the eluate and solid concentration of inorganic salts and heavy metals below the limiting values. The process conditions (in particular temperature, gas atmosphere, residence time) are adjusted in such a way that these pollutants are either evaporated and are therefore not present in the ash or are strongly mineral-bound in such a manner that they no longer leach out. Results concerning the behaviour of heavy metals and salts are available from experiments performed in batch operation on laboratory scale, i.e. using small charges (several g to kg). In order to be able to transfer this knowledge into practice and to optimize the process on a

large scale, one has to determine the location and amount of heavy metal evaporation under realistic conditions, in other words in a continuously-operated pilot plant.

The heavy metal content is usually determined by sampling the total flue gas flow and a subsequent analysis of the gases. Detecting the heavy metals directly at the location of evaporation using conventional sampling and analysis is, due to the harsh conditions in the combustion chamber, particularly difficult. The analysis itself cannot be carried out on-line. In addition, a very complex measurement network is necessary for an investigation covering the complete firing bed surface.

The radiotracer method provides the opportunity to follow the behaviour, location and concentration of a certain heavy metal species on-line during the entire combustion process in a technical waste treatment plant. When the combustion process in a grate system on the pilot plant-scale is used as an example, the following quantities can be determined with this method:

- the location of the heavy metal evaporation,
- the time course of the heavy metal evaporation,
- the amount of heavy metal evaporated.

The investigations discussed here were carried out in a pilot plant-scale forward-acting grate at the Clausthaler Umwelttechnik Institut GmbH (CUTEC) in Clausthal-Zellerfeld. Figure 1 shows the grate and the combustion chamber as the main components of the plant. The plant has a thermal capacity of 0.4MW, so a transfer of the results obtained to the industrial scale possible. A model fuel, consisting of 60 mass-% wood,

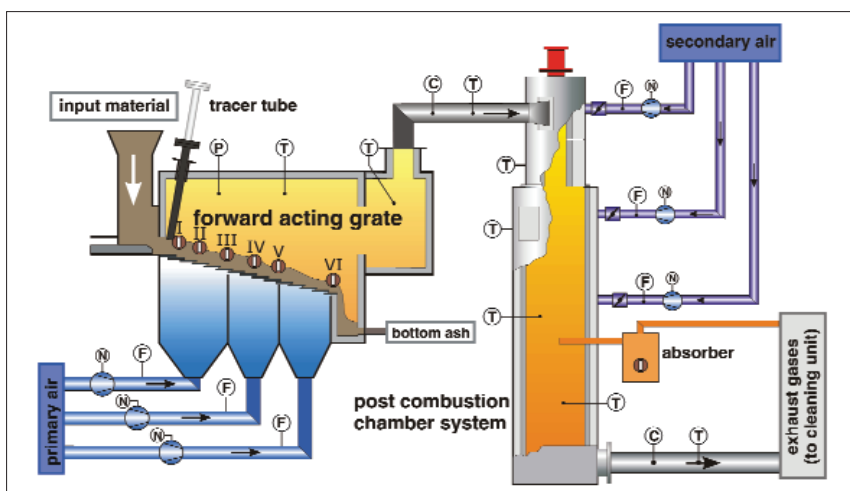


Fig. 1: Technical flowchart of the forward-acting grate plant (D radiation detector)

30 mass-% lava, and 10 mass-% RDF (refuse derived fuel), was used for the investigations. The pilot plant was operated steady-state with a fuel mass flow of 60 kg/h.

Out of the many elements of interest, copper and zinc were selected for the investigations in the pilot plant. Copper is representative of the nearly nonvolatile elements and zinc of a species which can be easily evaporated under certain conditions.

^{64}Cu and $^{69\text{m}}\text{Zn}$ ¹ were used as tracers for copper and zinc, respectively. The radioactive isotopes were generated by irradiation of metallic granules of ^{63}Cu or ^{68}Zn in the research reactor BER II. The tracer (^{64}Cu and $^{69\text{m}}\text{Zn}$ in different experiments), embedded in a RDF-pellet, was given into the plant as a short pulse (a so called DIRAC-impulse) by a special tracer tube (Fig. 1). Narrow-collimated and well shielded radiation detectors located along the sides of the grate registered the time course of the tracer concentration in the waste mass flow at different positions. They allowed for a determination of

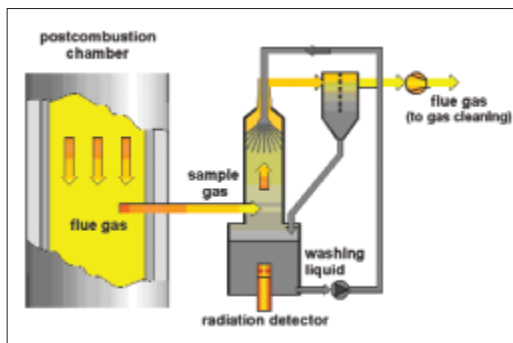


Fig. 2: Scheme of the absorber for the washing of the partial gas flow and quantification of the amount of heavy metal tracer evaporated

the location of the marked heavy metal species during the entire residence time in the solid bed. The heavy metals evaporated during the combustion process and carried out of the combustion chamber with the flue gas are caught to a certain degree by the absorber (Fig. 2). A radiation detector in this absorber registers the temporal concentration course of the heavy metal tracer evaporated. Since the collection of measured values by all detectors was started simultaneously with the introduction of the tracer, concentration changes in the time course of the measured signal at the absorber detector in the range of the combustion chamber could be assigned and the heavy metal evaporation could then be localized in the solid bed.

The quantification of the amount of heavy metal evaporated was made possible by a calibration of the absorber detector signal.

Figure 3 and Fig. 4 show exemplary the results of a copper and zinc evaporation experiment, respectively. The lower diagrams in the figures show the measuring results of the detectors positioned alongside the grate, the upper diagram the time course of the absorber detector signal.

In all experiments, a copper evaporation of 3 or 5% could be established. As can be seen in the upper diagram in Fig. 3, the evaporation takes place continuously during the entire tracer residence time on the grate. In contrast, an almost complete zinc evaporation could be observed, which takes place within a time period of a few minutes in a narrowly restricted section of the grate, in the section in which the local reducing conditions prevail.

Due to the fluctuations of heavy metal content and specification in the waste, clearer results could be obtained with the help of radiotracer measurement than by means of a classical mass flow analysis.

The project was financially supported through the Schweizerischer Nationalfonds (Swiss national fund), whom the author would like to thank.

¹ The letter m in the superscript indicates the metastable state of an isotope.

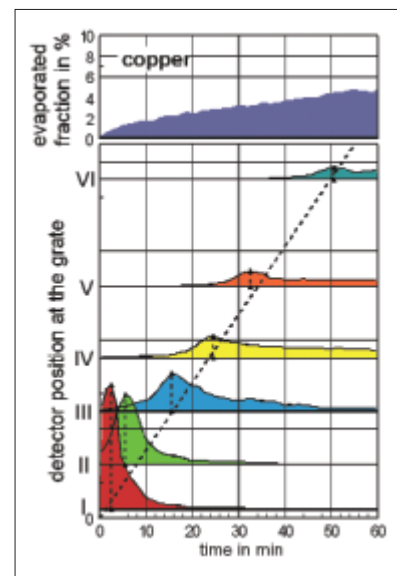


Fig. 3: Results of a copper evaporation experiment

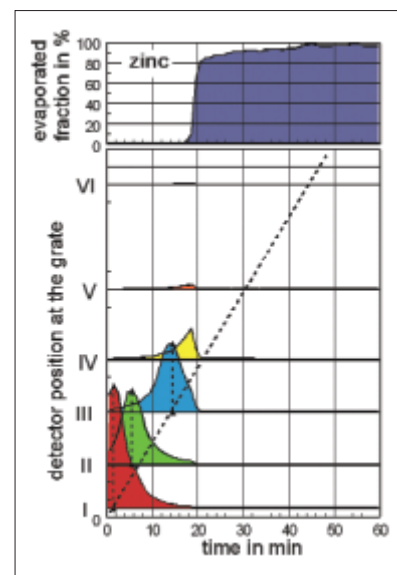


Fig. 4: Results of a zinc evaporation experiment

Corresponding author:

T. Jentsch

thorsten.jentsch@izfp-d.fraunhofer.de

Ordering upon melting dynamically enhanced

O. Russina¹, A. Triolo², F. Mezei¹, M. Russina¹

■ 1 HMI, SF1 ■ 2 Istituto per i Processi Chimico-Fisici, C.N.R., Messina, Italy

To understand the relation between molecular structure, dynamics and properties in non-crystalline matter [1] is of great current interest in nanoscale phenomena. Indeed, macromolecular systems, such as polymers and biopolymers are examples of pronounced local structures on the nanoscale, as shown in Fig. 1 by the neutron diffraction pattern measured in deuterated atactic polypropylene (DaPP), a representative of the class of polyolefins. Due to its chemical architecture, this form of polypropylene is fully amorphous over its thermal stability window. Accordingly, it is an ideal model system to investigate the correlation between structure and dynamics in amorphous materials. The local range order appears as a peak around 3.2 \AA^{-1} in the structure factor $S(Q)$ and reflects the atomic space correlation between close neighbours inside the chain (intra-chain order). The nearest neighbour interchain distance is reflected in the peak around 1.1 \AA^{-1} (interchain order).

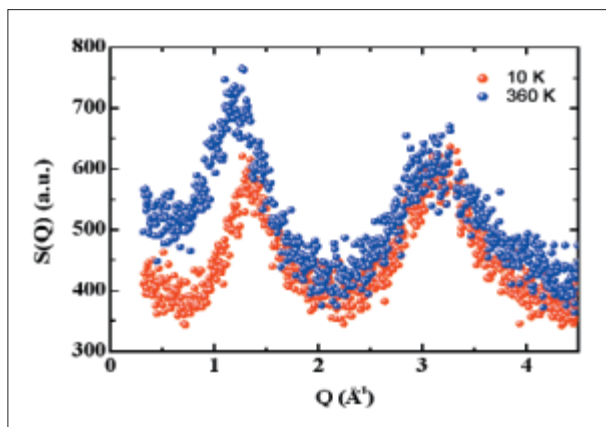


Fig. 1: Structure factor, $S(Q)$, of DaPP at two selected temperatures, below and above the glass transition ($T_g = 280 \text{ K}$). Data were collected at the E9 diffractometer

While the intramolecular peak does not change significantly with temperature, the intermolecular peak moves to smaller Q values and its amplitude increases with temperature. This shift of the peak position is mainly related to thermal expansion density change. However, the rise of its amplitude is remarkable and indicates an increase of the interchain correlation in the melt state (360 K) as compared to the glassy one (10 K). This strong increase of order upon heating and melting is very much in contrast with the usual notion that order is reduced by thermal motion.

Inelastic neutron scattering allows us to observe the evolution of this order in time via the determination of the dynamic structure factor, $S(Q, \omega)$. Here as the wave number Q is related to the distance as $r \sim 2\pi/Q$, the energy ω is related to the time by the relation $t \sim 1/\hbar\omega$. DaPP was investigated at the time-of-flight spectrometer NEAT. $S(Q, \omega)$ was measured at different temperatures ranging from the glassy state (20, 150 and 200 K) to the melt (300 and 340 K). After standard corrections (subtraction of background and correction for absorption) the data were corrected for multiple scattering in order to achieve the “real” scattering function. A selection of these data is presented in Fig. 2.

The intensity of the elastic peak forms the long time (*elastic*) structure factor $S_{el}(Q)$, showing the order that survives rather long times of about 0.1 ns. The temperature dependence of $S_{el}(Q)$, presented in Fig. 3, shows that the long-time interchain order decreases as usual with temperature.

The time of flight data, $S(Q, \omega)$, in Fig. 2 evidence a strong increase of the scattering intensity in the small energy exchange range ($\Delta E < 1.5 \text{ meV}$). This scattering is associated with correlations over characteristic times in the picosecond range and its existence is a general feature of dynamics in glass formers. We determined the structure factor associated with these dynamic correlations $S_{\text{inel}}(Q)$ by integrating $S(Q, \omega)$ between 0.04 and 1.1 meV, as shown in Fig. 3. The peak of $S_{\text{inel}}(Q)$ around 1.1 \AA indicates that contrary to the longer time correlations, the interchain order on the picosecond scale increases with increasing temperature, and it explains the anomalous increase of this order shown in Fig. 1. Thus we conclude that the surprising increase of the nanoscale order with increasing temperature in this polymer – even more surprisingly – is due to enhanced order on the picosecond time scale between much shorter times of atomic vibrations and the time limit $t > 0.1 \text{ ns}$, for which conventional macroscopic behaviour is observed. We believe that this radically new phenomenon of dynamically enhanced order with increasing temperature is an important clue to understand glassy systems.

*The main consequence of this finding is that the higher degree of order observed in the melt (as compared to the glassy state) has a **dynamic nature**, arising from the correlation of atomic motions over a time scale of order of the characteristic time of the fast dynamics (picosecond regime). While the static structure (with infinite lifetime) decays, the fast atomic motions are correlated.*

In conclusion, by using complementary neutron scattering techniques, we provided a novel interpretation for the concept of order in glass forming materials.

Acknowledgements

We should like to thank Dr. D.M. Toebbens for his support during the measurements at the E9 diffractometer.

[1] See e.g.: N. McCrum, B. Read, G. Williams, *Anelastic and Dielectric Effects in Polymeric Solids*; Wiley: London (1967)

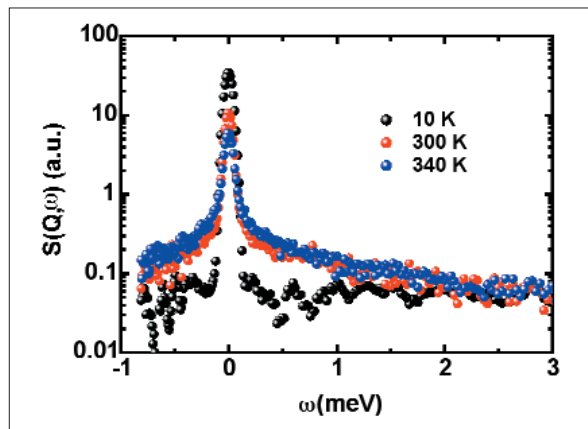


Fig. 2: Selected time of flight data of DaPP, $S(Q, \omega)$, collected at the NEAT spectrometer, at $Q_{\text{elastic}} = 1.6 \text{ \AA}^{-1}$

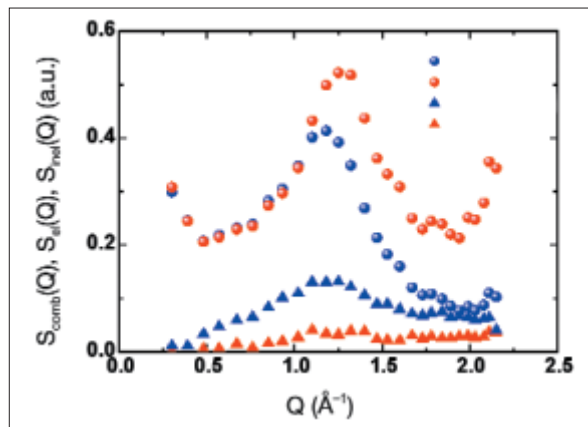


Fig. 3: Temperature dependence (red symbols for $T=20 \text{ K}$, blue symbols for $T=300 \text{ K}$) for the different structure factors defined in the text (see the text for details)

Search for scission neutrons using angular correlation method

E. Korobkina¹, R. Golub¹, T. Wilpert¹, G. Danilyan², A. Fedorov², I. Karpikhin², V. Krakhotin², V. Pavlov²,
 ■ 1 HMI, SF1 ■ 2 A.I. Alikhanov Institute for Theoretical and Experimental Physics, Moscow, Russia

More than 65 years ago Otto Hahn, Lise Meitner and Fritz Strassmann discovered the nuclear fission process. Nevertheless, today we still do not know very much about some of the fundamental aspects of fission. For example – we know that fission of the nucleus is accompanied by the emission of prompt neutrons (PFN). The angular distribution of such neutrons relative to the fission axis can be described at least by two components: most of them are elongated along the fission axis, while another part shows approximately a spherically symmetric distribution. It is evident that the former is evaporated by accelerated fission fragments because the elongation can be the result of kinematics only. But what is the nature of the second part? A spherically symmetric distribution means that the neutrons are evaporated by the nucleus before rupture of the neck at the scission point. So they were called *scission neutrons*.

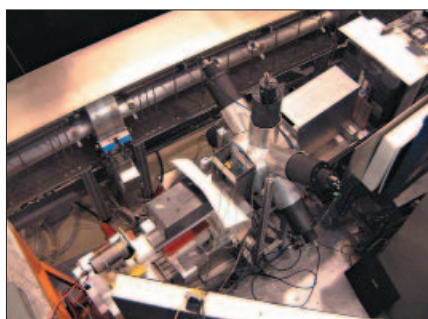


Fig. 1: A general view of the experiment on the cold neutron beam V13 during the adjustment of the set-up in 2003

Now we must mention that there is one exotic mode of fission, which is called *ternary fission*. This is the fission into two fragments accompanied by the emission of a charged light particle as p, d, t, ³He, ⁴He, ³He and so on. The angular and energy distribution of these particles shows that

they are emitted from the region between the two fragments. Most models of ternary fission describe it as evaporation from the neck at the scission point. But why does ternary fission not include neutrons? The evaporation of a neutron is easier than of a proton because for the former there is no Coulomb barrier. Is a scission neutron the neutral component of ternary fission? This is not easy to answer because in experiments it is practically impossible to distinguish between them and fragment neu-

trons due to the overlap of the energy-angular distributions. A lot of analysis has been performed to evaluate the probability of scission neutron evaporation. The estimates of the ratio of scission neutron to the total number of PFN vary from 1% to 35%! It is a result of arbitrary assumptions made in different analyses (see review in [1]). Thus it is high time to work out an alternative method to search for the scission neutrons.

It is well known that any angular correlation is a result of the interference of angular momenta. So because this is a quantum-mechanical effect, both, the magnitude and the sign of the correlation coefficients depend on the quantum numbers of the initial and final state as well as on the quantum characteristics of the outgoing particle. When the condition of the experiment does not allow us to choose a definite quantum state (initial or/and final), the observables will be the result of averaging over all N states involved in reaction. It means that any coefficient will be suppressed by a factor $1/N^{1/2}$. Concerning the fission process, it must be emphasized that the number of fragment's final states is an order of 10^8 . Therefore any angular correlation of particles emitted by fragments will vanish. In contrast, the number of initial and final states of the scission neutron should be rather small because they are evaporated by a cold, strongly deformed fissile nucleus. Thus a scission neutron can possess a non vanishing angular correlation with the spin of the compound nucleus. This is the main idea of our new approach to how to distinguish between scission and fragment neutrons.

It is well known that due to the weak interaction nuclear states do not possess a definite parity [2]. Therefore, there is always a P-odd term in the angular distribution of any particle emitted from an excited state of the nucleus. We decided to measure the P-odd asymmetry, i.e., a correlation between the momentum of scission neutrons, \mathbf{n}_{sc} , and the incident beam polarization, σ_{in} :

$$W \sim \{1 + A_{sc}(\sigma_{in}, \mathbf{n}_{sc})\}.$$

In reality we detect all prompt fission neutrons, because we cannot distinguish between them. Fragment neutrons imply the background that decreases the observable asymmetry. The magnitude of suppression depends on the angle relative to the fission axis. This angular dependence can be used to estimate the relative part of the scission neutrons.

The experiment is running on the polarized cold neutron beam V-13 with intensity $10^7 \text{ s}^{-1} \text{ cm}^{-2}$ (see Fig. 1). The layout of the experiment is shown in Fig. 2. Scintillation detectors detect both prompt fission neutrons and gammas. To distinguish between them we use a *time-of-flight* technique. Start comes from the fragment detectors in the fission chamber and stop comes from the neutron detector. On the TOF spectrum (Fig. 3) one can see both, gamma (narrow) and neutron (wide) peaks. The former are used to test systematic, because there is no P-odd asymmetry of γ -quanta emitted from fragments.

Our data taking during 2004 results in the following values of neutron and gamma asymmetry (both measured at 90° relative to fission axis)

$$A_n = (+2.7 \pm 0,8) \times 10^{-5}$$

$$A_\gamma = (-0.1 \pm 0,6) \times 10^{-5}$$

Thus we indeed have observed a pronounced effect for neutrons and no asymmetry of the gamma quanta.

Taking into account that the expected value of P-odd asymmetry of scission neutrons is of the order of 10^{-4} , our preliminary result means that the relative amount of scission neutrons is about 25% [3]. This is already the second angular correlation found for prompt neutrons [4]. It is extremely surprising and challenging for the theory of fission. Nevertheless, the present asymmetry value still has to be measured at different angles to allow more reliable evaluation. This is planned for 2005.

- [1] N.V. Kornilov, A.B.Kagalenko, F.-J. Hamsch, *Physics of Atomic Nuclei* **64**, 1373–1385 (2001); *ISINN-7*, Dubna, 241–248 (1999)
- [2] G.V. Danilyan, *Soviet Physics – Uspekhi* **23**, 323–330 (1980)
- [3] E.V. Brakhman, G.V. Danilyan, A.V. Fedorov, I.L. Karpikhin, V.A. Krakhotin, V.S. Pavlov, R. Golub, E.I. Korobkina, T. Wilpert, *JETP Lett.* **76**, 837 (2004)
- [4] G. Danilyan, *et al.*, *JETP Lett.* **76**, 697–699 (2002)

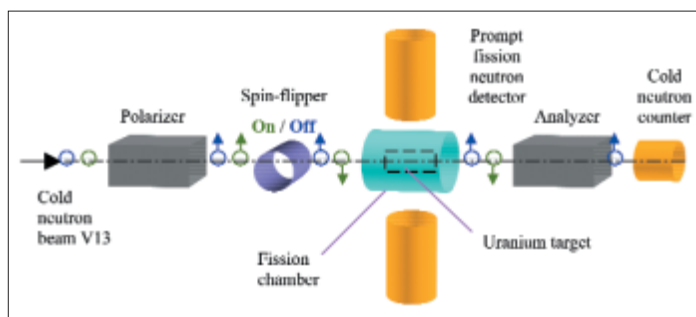


Fig. 2: Experimental layout. First cold neutrons are polarized vertically by a polarizer; then they pass through a spin-flipper, which reverses the polarization once per second. A large area uranium target inside the fission chamber is aligned along the beam. Fission fragments are detected by two sets of avalanche counters in the horizontal plain and prompt fission neutrons are detected by plastic scintillator detectors in the vertical plain relative to the beam axis. The analyzer and neutron detector behind the fission chamber are used to monitor both, neutron polarization and beam count rate.

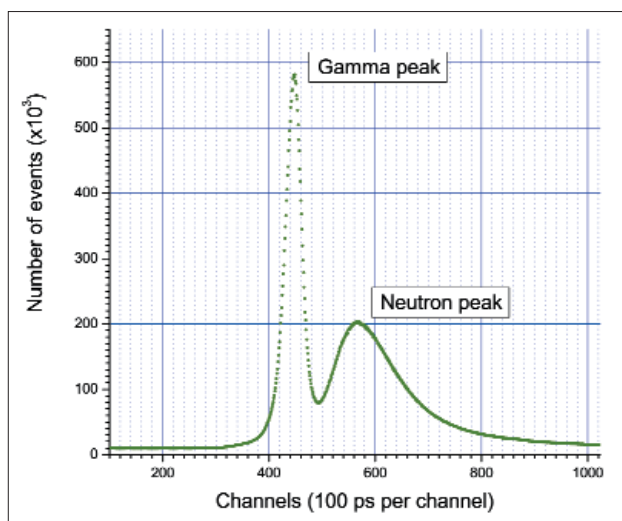


Fig. 3: Time-of-Flight spectrum of a neutron detector. The neutron detector does not only detect prompt fission neutrons but also the prompt fission gamma radiation. To distinguish between them, the difference in neutron and gamma-quantum velocities is used, i. e., a *time-of-flight* technique with a *start* from fragment and *stop* from a gamma or neutron. In the delay time spectrum one sees the narrow gamma-peak and the wide pike of prompt fission neutrons.

Corresponding author:

E. Korobkina
korobkina@hmi.de

Superconductivity? Just add water!

D. N. Argyriou¹, C. J. Milne¹, A. Chemseddine², N. Aliouane¹, J. Veira¹, S. Landsgesell¹, D. Alber³

■ 1 HMI, SF2 ■ 2 HMI, SE4 ■ 3 HMI, SF6

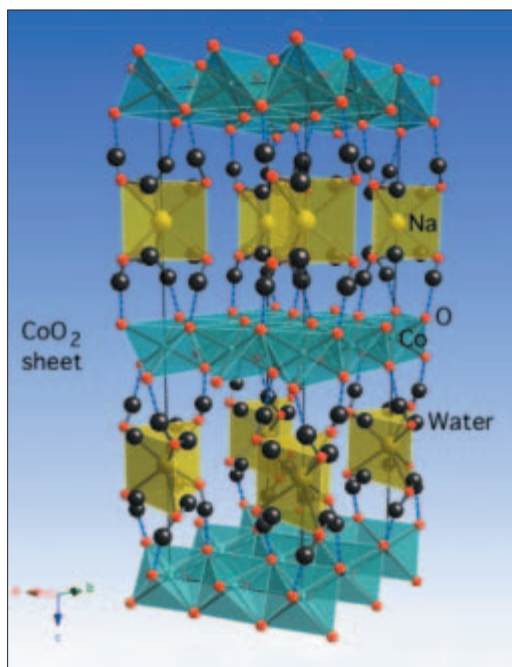


Fig. 1: The crystal structure of superconducting $\text{Na}_{0.3}\text{CoO}_2 \times 1.3\text{H}_2\text{O}$ determined using neutron powder diffraction at the Hahn-Meitner-Institut. [5] Our work found that Na is surrounded on average by six water molecules as shown in the figure forming triangular prisms with Na at the center and Oxygen (from the water) at the corners.

Superconductivity, the passage of electrical current with no resistance, is a unique phenomenon in physics exhibited by a relatively small number of materials at low temperature. Because of this unique property, superconducting materials can be used in a huge array of different applications from MRI scanners to particle accelerators. Researchers are constantly searching for new superconducting materials in the hope of increasing their T_c , the temperature below which they become superconducting. These searches sometimes yield surprising results. Recently Takada [1] from the National Materials Science Institute in Japan discovered that if he intercalates water between the CoO_2 and Na layers, in the oxide $\text{Na}_{0.3}\text{CoO}_2$ this material becomes superconducting.

At the Hahn-Meitner-Institut, we have examined the chemistry and structure of this new superconductor in great detail to understand how it becomes a superconductor. We hope that what we learn from this will help the search for better superconducting materials.

Electrons vs Holes

For an oxide material to become superconducting we first need to inject it with charge carriers, electrons or holes (lack of electrons), so an electrical current can pass through the material. Whether the charge carrier is an electron or hole is very important for the physics, as these two entities have different masses (the mass of the electron vs the mass of nothing!). The amount of charge carriers one can inject in to the material is called the electronic doping. These carriers are injected into the CoO_2 layer, the layer that is thought to conduct electricity.

A characteristic feature of the cuprate superconductors, materials with the highest known T_c (165 K), is the existence of an optimal electronic doping that gives a maximum superconducting transition temperature. This composition separates the underdoped and overdoped regimes in which T_c decreases from the optimal value. This behaviour is thought to be a universal characteristic of cuprate superconductors that arise from the fundamental origin of superconductivity for these oxides. The highest T_c is achieved when the CuO_2 sheets are doped with holes (about 0.15 to 0.3 holes for every Cu atom).

To test if this idea also holds for these new superconductors one needs to measure T_c as a function of the electronic doping. In these hydrate superconductors it was first thought that this could be done by varying the amount of Na between the CoO_2 sheets [2]. If one considers as a base line the amount of electrons for Co^{4+} (5 electrons), each Na atom will add 1 electron per Co-atom in addition to the 5 electrons of Co^{4+} (LS: t_{2g}^5). However, Takada found that the chemistry was not so simple, and Na alone does not control the number of charge carriers that are injected into the CoO_2 sheet [3]. He realized that along with water that is interlaced between Na and CoO_2 sheets (see Fig. 1), there are also H_3O molecules. A H_3O molecule looks like water in many ways, but it has one extra H-atom which is charged and therefore donates an additional electron. As a result the superconducting phase diagram had to be rethought completely.

At the Hahn-Meitner-Institut we synthesized a large number of samples and measured the valence of Co directly using chemistry [4]. What we found was very surprising and told us that these materials are indeed very similar to the cuprate superconductors. We found that superconductivity is achieved when holes are added to CoO_2 layer, and not electrons as it was originally thought [2]. In fact if we use as base line Co^{3+} , that has 6 electrons in its outer core (LS: t_{2g}^6), each Na and H_3O together act to remove one electron from Co^{3+} , thus injecting a hole in the CoO_2 layers. There is some very complex chemistry that occurs between the Na and the water so that changing significantly the amount of Na between the CoO_2 sheets it affects significantly the amount of H_3O^+ that enters the material.

We find that optimum T_c is achieved over the cobalt valence range of 3.24–3.35, while T_c decreases for valence states >3.35 (see Fig. 2). This is in stark contrast to the previous measurements by Schaak et al. [2] in which it was assumed that Na alone sets the electronic doping. Our work, in contrast, demonstrated that these materials are hole doped with respect to Co^{3+} . Also the width of the region where superconductivity occurs looks to be very similar to the cuprate superconductors. This work helps us understand that superconductivity for all its novelty and interest may be a more common state in matter than we previously thought. The search continues to find better materials so we can harness the opportunity that they offer.

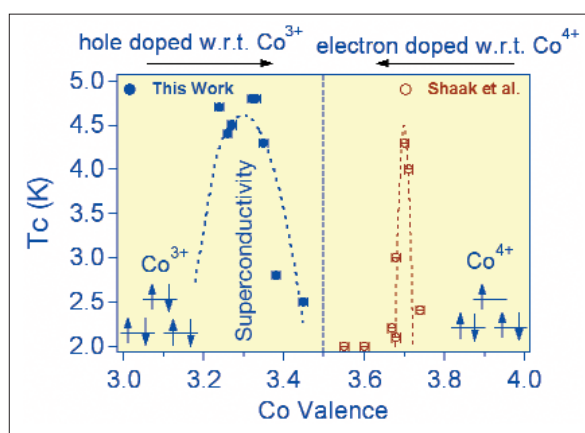


Fig. 2: The superconducting phase diagram of $\text{Na}_x\text{CoO}_2 \cdot y\text{H}_2\text{O}$, determined at the Hahn-Meitner-Institut

- [1] K. Takada, H. Sakurai, E. Takayama-Muramachi, F. Izumi, R. A. Dilanian, T. Sasaki, *Nature* **422**, 53 (2003)
- [2] R. E. Schaak, T. Klimczuk, M. L. Foo, R. J. Cava, *Nature* **424**, 527 (2003)
- [3] K. Takada, *et al.*, *J. Mater. Chem.* **14**, 1448 (2004)
- [4] C. J. Milne, D. N. Argyriou, A. Chemseddine, N. Aliouane, J. Veira, S. Landsgesell, D. Alber, *Phys. Rev. Lett.* **93**, 247007 (2004)
- [5] D. N. Argyriou *et al.* *Journal of Physics: Condensed Matter* (in press)

Corresponding author:

D. N. Argyriou
argyriou@hmi.de

Competition of two AF structures in UNiAl single crystal

K. Prokeš¹, E. Brück², V. Sechovský³

■ 1 HMI, SF2 ■ 2 Van der Waals-Zeeman Inst., University of Amsterdam, The Netherlands

■ 3 Dept. of Electronic Struct., Charles University, Prague, The Czech Republic

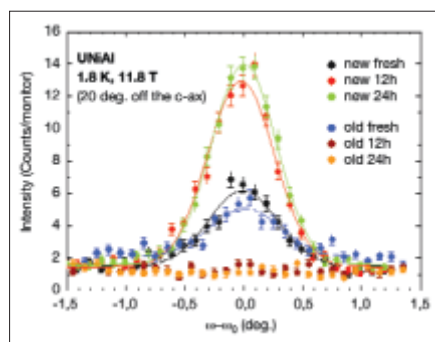


Fig. 1: Rocking curves through the new (1.173 0 0.5) and the old (1.1 1.1 0.5) magnetic reflections just after reaching 11.8 T (fresh) and after 12 and 24 hours

UNiAl forms in the hexagonal ZrNiAl type of structure and orders anti-ferromagnetically (AF) below $T_N=19.3$ K. Below T_N , new Bragg peaks due to magnetic order appear that are indexable considering a propagation vector $q_{old}=(0.1 \ 0.1 \ 0.5)$ of the AF structure. The magnetic-structure refinement points to two U moments (amplitude of $1.28 \mu_B$) in the UNiAl unit cell coupled together ferromagnetically

and the third one, uncoupled due to symmetry, which is much smaller ($0.8 \mu_B$) [1]. When a magnetic field $H||c$ is applied at temperatures lower than $\approx 0.5 T_N$, UNiAl undergoes a sharp MT at $\mu_0 H_c \approx 11.35$ T (4.2 K) [2] towards a high field ferromagnetic (HFF) phase. Neutron diffraction experiments in magnetic fields confirmed the HFF phase with a unified U moment $\mu_U \approx 0.9 \mu_B$. Some time ago, magnetic history dependent phenomena were revealed in UNiAl, which concern all the bulk properties [3]. Original neutron diffraction studies suggested that below 7 K after applica-

tion of a magnetic field higher than about $8 \div 9$ T the original AF structure disappears and after releasing the field a new AF structure characterized by $q_{new}=(0.173 \ 0 \ 0.5)$ appears [4]. The difference between the “old” and “new” AF structures is that the sine-wave modulation of U moments (having the same amplitude) is along the [110] in the former and [100] in the latter case.

In order to study stability and competition of the two phases in the experimental arrangement with a small vertical opening of the magnet capable to produce sufficient magnetic field we had to turn the crystal by $\sim 20^\circ$ around the [100] direction in order to reach two characteristic magnetic reflections – namely (1.1 1.1 0.5) and (1.173 0 0.5); the former will be called “old” and the latter “new”. The study was performed on the triple axis spectrometers E1 and V2 and double-axis diffractometer E4 installed at the Hahn-Meitner-Institut Berlin using the incident wavelengths of 2.4, 4.6 and 2.4 \AA , respectively. Since the c -axis of the crystal in our experiment is deflected from the field direction (vertical axis) by $\sim 20^\circ$ the critical field to a ferromagnetic state is crossed at 12.14 T. However, Fig. 1 shows that the new AF state is established even after being exposed for ~ 12 hours to only 11.8 T, which confirms that we do not need to cross the B_C .

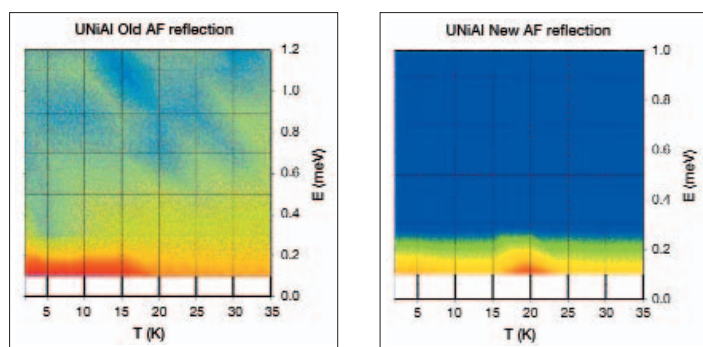


Fig. 2: Low-energy signal measured on V2 at the old (left: log scale) and new (right: linear scale) magnetic reflections at zero field upon cooling. Note significant signal around T_N in the case of the new reflection.

When decreasing the field to zero, intensities relax to their original values, however, much slower. No clearly defined excitations could be resolved up to 8 meV energy transfer in either of the phases. This is obviously due to the sine-wave modulation of U moments leading to a spread of the exchange energy. The response function in UNiAl consists of many contributions having small intensities and centered at different energy transfers.

In Fig. 3, we show the contour plots of the temperature dependencies of the quasielastic response function measured at the two characteristic reflections (old at the top) at various magnetic fields obtained on E1. As can be seen, the old AF structure remains stable in the whole temperature range in fields up to ~ 8 T. Above this field,

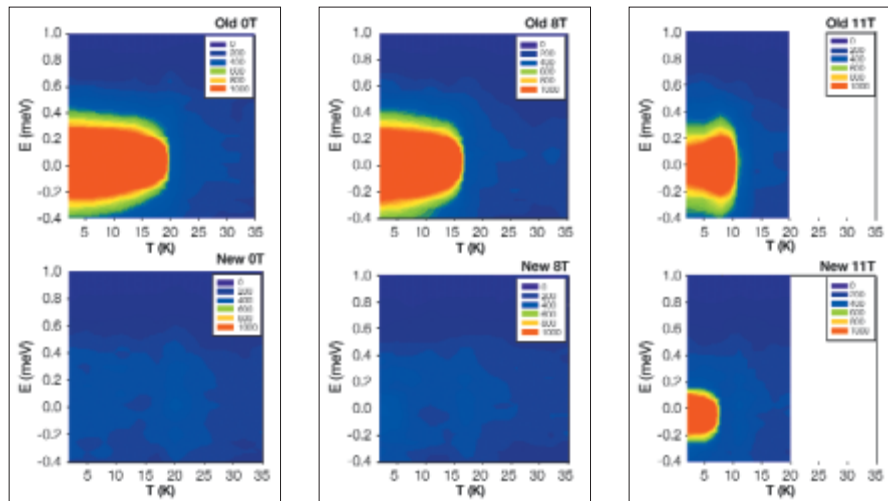


Fig. 3: Quasielastic signal measured on E1 at the old and new magnetic reflections at various applied fields (left – 0T, middle – 8T, right 11 T) upon cooling. Note significant signal around T_N (which decreases with field) and appearance of signal at lower temperatures in fields above 8 T at the new reflection (middle bottom).

the new AF structure begins to compete with the old one and above 11 T it becomes stable. Note the appearance of the “new” reflection at ~ 7 K upon the field of 11 T (about 4 K lower than the “old” reflection appears) and gradual disappearance of the “old” reflection at lower temperatures. This points to slow relaxation phenomena – due to thermal activation. Fact that the old reflection appears at higher temperature than the new one points to the existence of a second-order magnetic phase transition. Interestingly, a field of 11 T corresponds well with the field, above which the magnetic phase transition is of the first order type [2]. A significant intensity around T_N suggests that both AF structures compete even in zero-field around T_N . At the moment it is hard to reconcile the mechanism that is responsible for the change of the AF structure upon application of high magnetic field. One has to recognize that the AF coupling along the hexagonal axis (although in our experiments not parallel to the applied field, in previous experiments with $B//c$ axis the same phenomenon has been observed), the size of U magnetic moments and even the length of the sine-wave modulation within the basal plane remain in both AF structures unchanged. What is affected by the field is *in-plane* coupling direction that merely turns within the hexagonal basal plane and remains perpendicular to the field direction. In Fig. 4 we show the microscopic difference between the old AF structure and the new, established at high fields. In the original AF structure there are two kinds of zigzag chains, one, chain I, consisting only of U atoms, the other one, chain II, having the sequence U-Ni-U-Ni-. Moments in the latter chain are symmetrically not equivalent with those in the former chain. As the field is increased, all the moments become for some reason (a possible mechanism is mentioned below) equivalent and a new exchange path sets in. In the new high-field AF phase, all the

U moments are equivalent forming chain III with a sequence Ni-U-U-U-Ni-U-U-U-. Ab-initio calculations on isostructural compound UNiGa [5] (AF below 40 K) revealed a quite complicated topology of the Fermi surface with six-fold symmetry features in the basal plane that are alternated substantially upon application of magnetic field. At this point, we can only argue that a field driven modifications of the Fermi surface topology are responsible for this unique change of the AF structure in UNiAl. Theoretical ab-initio studies are necessary to elucidate this model.

- [1] K. Prokeš, F. Bourdarot, P. Bulet, P. Javorský, M. Olšovec, V. Sechovský, E. Brück, F.R. deBoer, A. A. Menovsky, Phys. Rev. B **58**, 2692 (1998)
- [2] V. Sechovský, L. Havela, in: *Handbook on Magnetic Materials*, ed. K.H.J. Buschow, (Amsterdam, North-Holland, 1998) Vol. 11, p. 1.
- [3] O. Syshchenko, K. Prokeš, E. Brück, V. Sechovský, Physica B: Condensed Matter, **312–313**, 879–881 (2002) and references therein
- [4] K. Prokeš, P. Javorský, A. Gukasov, E. Brück, V. Sechovský, Physica B: Condensed Matter, **312–313**, 872–874 (2002)
- [5] V.N. Antonov, A. Ya. Perlov, P.M. Oppeneer, A.N. Yaresko, S.V. Hallilov, Phys. Rev. Lett. **77**, 5253–5256 (1996)

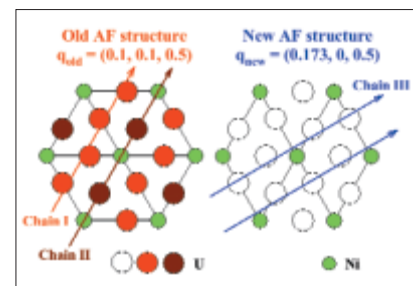


Fig. 4: Schematic representation of the “old” and “new” AF structures (one domain shown) of UNiAl showing different kinds of chains (shown by different shading) containing U ions

Metal foams

N. Babcsán^{1,2}, F. García-Moreno², B. Matijasevic², H. Helwig¹, A. Haibel¹, A. Rack¹, J. Banhart^{1,2}

■ 1 HMI, SF3 ■ 2 TU Berlin, Germany



Fig. 1: left: aluminium foam blown with air from a particle-stabilized melt and beer, right: zinc foam and bread roll, both foamed by internal gas creation (Photographs: Hahn-Meitner-Institut)

Introduction

Metal foams are challenging materials for both fundamental and applied research. They distinguish themselves from other materials by low density, high specific stiffness, and high-energy absorption capability. Therefore, they become increasingly popular for industrial applications. Like all other foams, metal foams are produced in the liquid state. Liquid metal foams, by definition, are collections of gas bubbles uniformly dispersed in a liquid metal separated by self-standing thin liquid films. Two methods for foaming metals, distinguished by the way the gas enters the melt, i.e. by the gas source, are used. Bubble creation can be *external* or *internal*. In the former case, gas bubbles are created by continuous gas injection. The foam accumulates at the surface of the melt and the result resembles a glass of draught beer. In the latter method, gas-releasing propellants – akin to the blowing agents of yeast used by bakers – are added to the melt or compacted powders (Fig. 1 and 2).

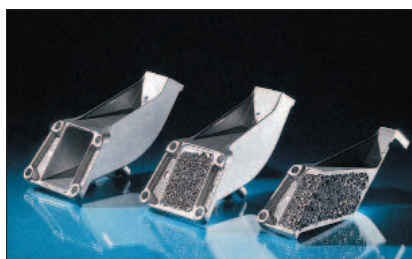


Fig. 2: Foamed part of aluminium dedicated for BMW engine mounting bracket (courtesy of HKB, Austria)

Several scientific challenges and industrial problems of metal foams give motivation for further research. From the scientific point of view, the evolution and the stabilisation of the liquids are in the focus, while industry is searching for process optimization and new metal foaming technology. Our group tries to

work in both the applied and the fundamental fields collaborating with scientists from Japan, Austria, USA and from spin-off companies.

In the following part, we detail the progress in understanding evolution, stability, 3D architecture and microstructure of metal foams. Only very recently, the issue of metal foam stabilisation was addressed and traced back to the presence of micro- or even nanometre-sized solid particles in the liquid metal [1]. The time has therefore come to understand liquid metal foams as an independent field of research and to look at these systems from the viewpoint of colloid chemistry.

Evolution of foams blown by using internal gas source

A compact microfocus X-ray source was used to monitor foam expansion kinetics while the temperature ramp and the TiH_2 blowing agent treatment were varied [2]. A new pressure furnace was built and used to carry out high pressure (<10 bar) and low pressure (>0.001 bar) experiments in oxidizing or inert atmospheres. A strong influence of the gas pressure on the foaming behaviour was found (Fig. 3). Under low pressures, high coalescence, instabilities and rising big bubbles characterise the foaming. Under high pressures, besides a reduced expansion, an extremely small average cell size and high homogeneity were observed. Release from high pressure to normal pressure led to an increased expansion. Also reversible expansion and compression after several pressure cycles were found with a flexible cell wall structure. An additional expansion with high coalescence followed each cycle increasing the maximal expansion from $F/F_0 \sim 1.5$ at 8 bar to $F/F_0 \sim 4$ at 1 bar.

MS, TGA and XRD experiments showed that the decomposition of as-received TiH_2 powder in argon occurs in two stages [3]. Heating as-received TiH_2 at 10 K/min in argon leads to hydrogen release at 400°C. Heat treatment at 480°C for 180 min eliminates the first decomposition stage completely and increases the temperature at which gas evolution occurs. Oxide layers around the cores of the titanium-hydride particles formed during annealing in air act as very effective diffusion barriers. XRD and TEM experiments showed the formation of TiH_2 and Ti_3O during

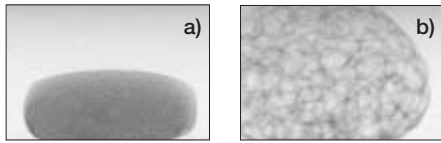


Fig. 3: X-ray radioscapy images of **a)** Al99.7+0.5 wt% TiH₂ foamed under 8 bar in air, **b)** additional expansion of **a)** after release from 8 bar to 1 bar with -0.2 bar/s

heat treatment. We have shown that results from different methods can be combined to form a more complete picture of decomposition of TiH₂ and that various methods provide complementary information.

Evolution of foams blown by external gas injection

External foam evolution strongly depends on the foaming gas being used. The use of an oxidizing gas, e. g. air, results in a thick (100 nm) oxide skin on the cell wall surfaces acting like a rigid stabilizing layer. The role of oxidation in liquid metal foams is revealed by ex-situ and in-situ analysis [4]. A new X-ray transparent foaming furnace was constructed adapting Metcomb technology. The furnace was also used for technology development with our industrial partner. In-situ experiments were performed using microfocus X-ray source at our laboratory at TU Berlin. When blowing Duralcan type metal matrix composites, the drainage and the coalescence rate were quantitatively monitored. Significant drainage was found within the first 20s of foam decay for argon-blown foam. In air-blown foams, drainage was hardly detectable. Isothermal holding leads to coarsening and a slight degradation of uniformity in argon-blown foams (Fig. 4) while air-blown foams remain almost unchanged even after 100 min. During solidification foams shrink significantly in both cases.

3D architecture and microstructure

Synchrotron tomography of aluminium and zinc foams has been carried out at BESSY and evaluated using 3D image analysis. The correlation between the blowing agent's particle position and the pores as well as the critical lamella thickness at different foaming stages were investigated. We obtained various correlations for different alloys, which indicates that the pore formation mechanism depends on the physical properties of the alloy to be foamed. The critical lamella thickness is in the same order of magnitude (20–30 μm) for both aluminium and zinc alloys [5].

Pore-particle correlations in SiC-particle stabilized internal foams were investigated. For the first

time, tomographic measurements of liquid metallic foams were performed. The results of the measurements clarified the rearrangement process of SiC particles during foaming. It could be shown that the accumulation process of the SiC particles on the pore surfaces takes place prevailing in the liquid state due to their partially wetting property. However, the process also continues during the solidification. It seems that due to the solidification front the particles were additionally pushed on the pore surfaces [6].

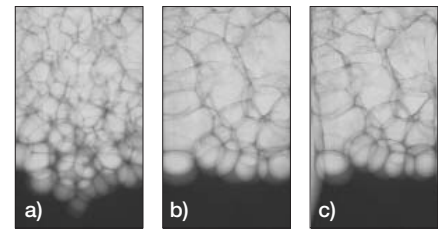


Fig. 4: X-ray radioscapy images of the evolution of argon-blown foam produced by gas injection. **a)** just after foam formation, **b)** at the end of isothermal holding (5 min), **c)** after solidification. Sample widths are 40mm at the bottom.

Future goals

- X-ray tomography with cone beam
- Comparison of foaming behaviour of tixocasted, hot compacted and hot extruded precursor metal powders
- Metallography investigation on single cell walls
- Surface tension measurement of liquid-metal colloids
- Fast radioscapy monitoring coalescence of single liquid-metal films

- [1] J. Banhart, *Manufacturing Routes for Metallic Foams*, Journal of Metals, **52**, 22–27 (2000)
- [2] F. Garcia-Moreno, M. Fromme, J. Banhart, *Real time X-ray radioscapy on metallic foams using a compact micro-focus source*, Adv. Eng. Mat., **6**, 416–420 (2004)
- [3] B. Matijasevic, S. Fiechter, I. Zizak, O. Görke, N. Wanderka, P. Schubert-Bischoff, J. Banhart, *Decomposition behaviour of as-received and oxidised TiH₂ powder*, in: Proc. PM2004 World Congress, Ed.: H. Danninger, R. Ratzl, EPMA, Vol. 4, pp. 149–155
- [4] N. Babcsán, D. Leitmeier, H.-P. Degischer, J. Banhart, *The role of oxidation in blowing particle-stabilised aluminium foams*, Adv. Eng. Mat., **6**, 421–428 (2004)
- [5] A. Rack, A. Haibel, A. Bütow, B. Matijasevic, J. Banhart, *Characterization of metal foams with synchrotron-tomography and 3d image analysis*, 16th World Conference on Non-destructive Testing, Montreal, 30.08.–03.09.2004
- [6] A. Haibel, A. Bütow, A. Rack, J. Banhart, *Quantitative analysis of pore-particle correlations in metallic foams*, 16th World Conference on Non-destructive Testing, Montreal, 30.08.–03.09.2004

Corresponding author:

N. Babcsán
babcsan@hmi.de

Magnetic anisotropy of Ni changed by extreme lattice expansion

Y. Manzhur¹, P. Imielski², K. Potzger¹, W.D. Brewer², M. Dietrich³, M.J. Prandolini^{1,2}, H.H. Bertschat¹

■ 1 HMI, SF4 ■ 2 Institut für Experimentalphysik (WE1), Freie Universität Berlin, Germany ■ 3 Technische Physik, Universität des Saarlandes, Saarbrücken, Germany and The ISOLDE-Collaboration, CERN, Genève, Switzerland

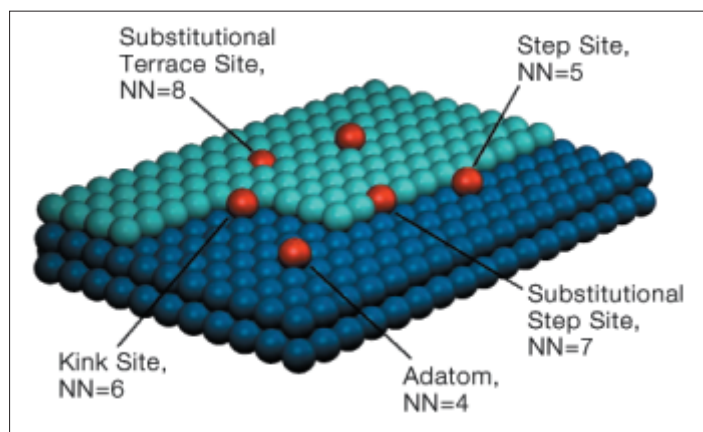


Fig. 1: Idealised surface of a single crystal with (001) orientation, the two shades of blue represent a surface step, radioactive probes are shown in red. All possible regular lattice sites for the impurity atoms as local probes are indicated. The probe atoms can be differentiated by the number of nearest Ni neighbours (NN).

One important new property afforded by ultrathin 2-dimensional magnetic films is perpendicular magnetic anisotropy (PMA). Presently, almost all magnetic recording of digital data uses conventional longitudinal (in-plane) magnetic materials. One method in order to achieve ultrahigh density magnetic recording (in the Tbit/inch² range) is the use of a medium which is magnetized perpendicular to the plane. The aim of this study is to investigate the structure and magnetic anisotropy of ultrathin Ni films, with a bulk lattice parameter of 3.52 Å, grown on Pd(001), with a considerably larger bulk lattice parameter of 3.89 Å. The experiments were conducted using perturbed angular correlation (PAC) spectroscopy in the ultra-high-vacuum (UHV) chamber ASPIC (Apparatus for Surface Physics and Interfaces at CERN).

Ultrathin films of Ni grown on non-magnetic substrates generally have in-plane surface anisotropy [1]. However, the bulk magnetostriction constant λ_{001} for Ni is negative compared to positive values found for Co or Fe. Thus, per-

pendicular magnetism would be possible for ultrathin Ni(001) films, if it would be possible to apply a large enough compressive stress to the film resulting in a negative strain in the [001] direction. This can be achieved *artificially* by growing ultrathin Ni films on non-magnetic substrates with a larger lattice constant and assuming coherent pseudo-morphological growth, as was demonstrated by growing ultrathin Ni films grown on Cu(001) where, however, the lattice mismatch is only 2.5% [2]. In this system, below a critical thickness $d^* = 7$ monolayers (MLs), the ultrathin Ni films were found to be in-plane, where the (in-plane) surface anisotropy dominates for small d , above this critical thickness, the magnetisation was found to be dominated by the magnetoelastic term and therefore is perpendicularly magnetised. Ni grown on Pd(001) is known to grow also pseudo-morphologically, with a lattice expansion of 10.4% up to 6 MLs [3], thus we expect that with greater lattice expansion, the critical thickness d^* at which Ni comes out of the plane would be reduced.

The magnetic alignment of the ultrathin Ni film on Pd(001) was measured with radioactive ^{111m}Cd probe atoms, sitting on the (001) surface, called an “adatom” with 4 next nearest Ni neighbours (NN), see Fig. 1, since the induced magnetism in the Cd atom is expected to be collinear to its next nearest Ni neighbours [4]. All other possible surface sites of a (001) surface are also shown in Fig. 1, the magnetic response of Cd probes sitting at these other sites were measured by previous studies [4].

Radioactive ^{111m}Cd probe atoms are provided by the on-line isotope separator ISOLDE at CERN, see Fig. 2. They are produced by bombarding a liquid Sn target with 1.2 GeV protons. Following mass separation in a magnetic field, they are transferred by a UHV beam-line and are implanted in a catcher-foil in the chamber, ASPIC. The soft-landing of these radioactive probes onto the sample occurs through a two stage resistive heating process.

The sample was prepared by molecular beam epitaxy (MBE) growing 2 atomic monolayers (ML) of Ni on Pd(001) at room temperature. Structure studies showed a coherent pseudomorphological Ni growth, with Ni having an out-of-plane tetragonal distortion, i.e., +10.4% expanded in the plane, and according to a simple linear elastic model, compressed by -13.3% in the out-of-plane [001] direction, as shown in Fig.3. Thereafter, the sample was cooled to 40K and a small amount of radioactive ^{111m}Cd probe atoms were soft-landed onto the surface, and a PAC spectrum was taken of the sample.

At a sample temperature of 40K, there is no diffusion of the Cd atoms across the surface and only one dominant site was found, i.e., adatoms with 4 next nearest Ni neighbours (NN), see Fig. 1. The probe nuclei experienced magnetic hyperfine fields (B_{HF}), resulting in discrete PAC frequencies. The magnitude of the B_{HF} was found to be 30% smaller than for an adatom on a pure Ni surface (7 Tesla) in accordance with theoretical predications. However, important for this measurement, the angle of the magnetic hyperfine field was found to be canted 40° out of the plane. Thus there is a significant change in the magnetic anisotropy for ultrathin Ni films with extreme lattice expansion.

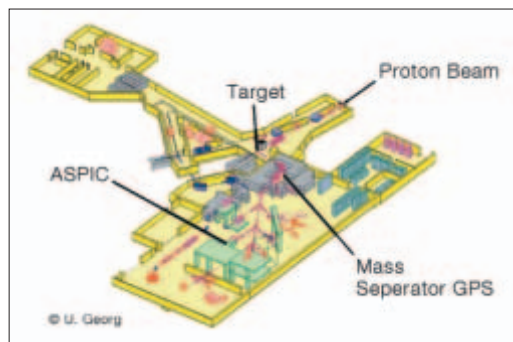


Fig. 2: The on-line mass separator ISOLDE at CERN. The ultra-high vacuum (UHV) chamber ASPIC (Apparatus for Surface Physics and Interfaces at CERN) is located in the center of the experimental hall. It is connected to the mass separator by a UHV beam line. (Courtesy of U. Georg, ISOLDE)

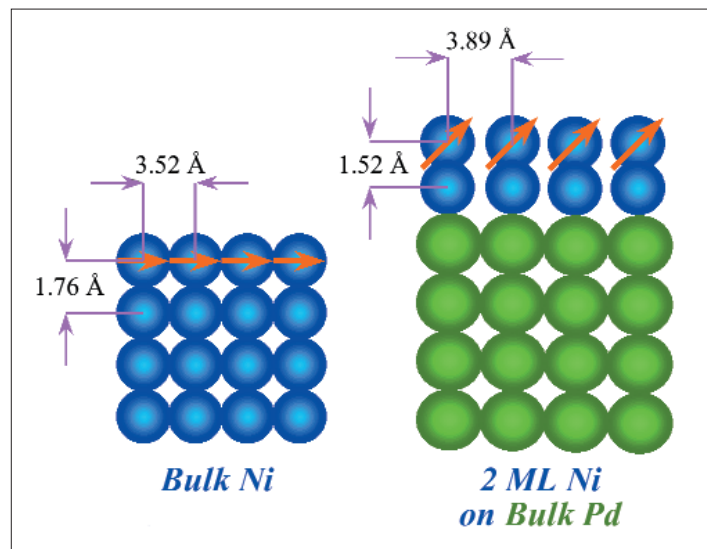


Fig. 3: Lattice parameters are shown for a bulk Ni single crystal surface (blue), the Ni surface magnetisation is in the plane, shown by the red arrows (left). However, 2 MLs Ni grown on Pd(001) is lattice expanded in the plane and compressed in the out-of-plane direction, the magnetisation was measured to be canted out of the plane (right).

Since the surface anisotropy scales as $1/d$, 2 MLs of Ni could be expected to be dominated by the in-plane surface anisotropy as was found for Ni on Cu(001), however, Ni, with a lattice expansion of 10.4% on Pd, would have a greatly enhanced magnetoelastic term causing an out-of-plane magnetisation. An estimate for this energy is 1470 kJ/m , which is about 4 times greater than measured for Ni grown on Cu [2]. As a result, this anisotropy dominates, causing a canting even at 2 ML of Ni, as shown in Fig. 3.

- [1] W. J. M. de Jonge, P. J. H. Bloemen, F. J. A. den Broeden, in *Ultrathin Magnetic Structures 1*, ed. J. A. C. Bland and B. Heinrich (Springer, Berlin, 1994) Chap 2.3.
- [2] B. Schulz, K. Baberschke, *Phys. Rev. B* **50**, 13467 (1994)
- [3] G. A. Rizzi, M. Petukhov, M. Sambri, G. Granozzi, *Surf. Sci.* **522**, 1 (2003)
- [4] K. Potzger A. Weber, H. H. Bertschat, W.-D. Zeitz, M. Dietrich, *Phys. Rev. Lett.* **88**, 247201 (2002)

Texture modification in nanocrystalline materials using swift heavy ions

I. Zizak¹, N. Darowski¹, G. Schumacher¹, S. Klaumünzer¹, W. Assmann², J. Gerlach³

■ 1 HMI, SF4 ■ 2 Ludwig-Maximilians-University Munich, Germany ■ 3 Leibniz-Institute for Surface Modification, Leipzig, Germany

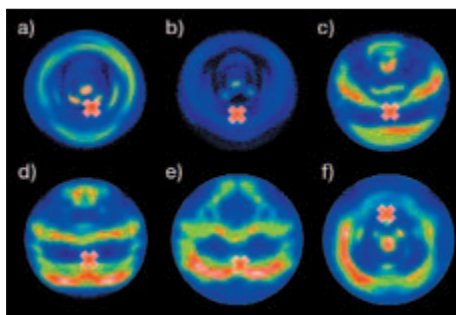


Fig. 1: Orientation distribution (texture) of the (101) planes in α -Ti layer after irradiation with different fluences.

a–e) In unirradiated sample the pattern is symmetrical around the normal to the sample surface. During irradiation with 350 MeV ions with different fluences we observe two changes: (I) the pattern moves upwards, (II) the ring structure disappears. The direction of the ion beam is marked with the red 'X'. The applied fluences are **a)** 1×10^{14} , **b)** 3×10^{14} , **c)** 7×10^{14} , **d)** 12×10^{14} , and **e)** 18×10^{14} ions/cm². **f)** If we take the sample irradiated with 7×10^{14} ions/cm² (**d**) and irradiate it with the same fluence in the opposite direction, the ring structure moves back. This means that the original texture was restored.

Introduction

In order to optimize the surface properties of materials for different applications without changing their bulk properties, one often coats them with thin layers of other materials. Physical vapour deposition (PVD) is a standard method used to produce thin polycrystalline layers. The size and the orientation of the grains created in this process depend on many process parameters, such as the deposition rate or the substrate temperature. When materials are deposited in micrometer thick layers, the grains have often sizes of 10–100 nm. Usually, the grains are not randomly oriented. Since different

lattice planes have different surface energies, during growth, the energetically favoured lattice plane is selected to be parallel to the surface. When there are no reasons for in-plane alignment, the orientation distribution of lattice-plane normals, denoted as texture, is symmetrical around the surface normal (fibre texture).

The material properties relevant for applications are strongly influenced by the layer texture. Mechanical properties, like wearing, depend on the packing density of the plane parallel to the surface as different lattice planes have different packing densities. Since the work needed to emit an electron depends on the surface properties, the electrical and, specially, the electro-optical properties are influenced as well.

The lattice plane preferred during the deposition need not be the best choice for applications. In the last few years, large effort was made to influence the orientation of the grains in deposited layers. One of the most promising methods is the ion beam assisted deposition (IBAD), where layers are irradiated with low-energy ions during deposition. The direction of the ion beam introduces a second preferred axis in the energy of the deposited layer leading to a crystallite orientation-distribution different from the unirradiated case.

Recently, we measured a change in orientation of the grains in nanocrystalline vapour-deposited Titanium (Ti) layers after irradiation with high-energy heavy ions. Swift heavy ions deposit their energy in solids mainly through electronic interaction. Since collisions with solid nuclei are unlikely at high energies, ions travel through the solid on straight paths. The energy deposited by the ion is concentrated in a volume a few nanometers around the ion path.

Experiment

In our experiment, polycrystalline layers were irradiated with 350 MeV gold ions with different fluences of up to 10^{15} ions/cm². We studied systematically titanium and titanium nitride, varying the layer thickness, grain size, and crystal structure of the sample. The titanium crystal structures

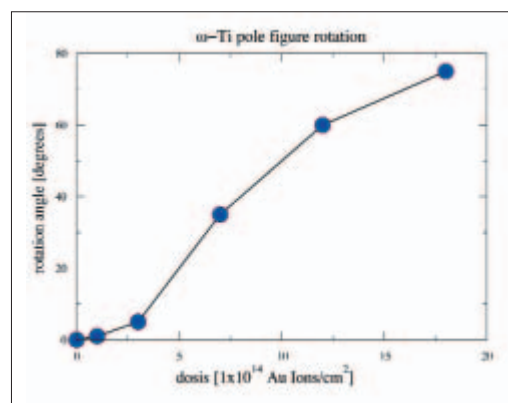


Fig. 2: Dependence of the angle of the grain rotation on the fluence

studied were in the hcp phase, which is stable under normal conditions (α -Ti), and in the complex hexagonal high-pressure phase, which is also created during irradiation (ω -Ti). TiN has the bcc crystalline structure, which is the same as the structure of rock salt.

Since a very high flux of high-energy ions was needed, the samples were irradiated at the Hahn-Meitner-Institut ion accelerator ISL. Different directions of the impinging ion beam were used.

The textures were determined at Hahn-Meitner-Institut's 6-circle diffractometer at the KMC2 bending magnet beamline at the Berlin synchrotron light facility BESSY. A combination of an area-sensitive detector and an intense synchrotron beam allowed for a very fast acquisition of the complete orientation distribution in the sample.

Results

In our experiment, layers with different compositions showed apparently different kinds of behaviour. In coarse-grained materials, no changes in the orientation distribution were observed. In different nanocrystalline materials, the orientation changed in different ways. In α -Ti, the rotational symmetry around the surface normal disappeared, and the grains aligned with one preferred axis towards the ion beam [1]; in ω -Ti the texture continuously rotated away from the ion beam. In TiN layers both effects were observed simultaneously.

Although the correlation between the crystalline axes and the impinging ion beam direction (as in α -Ti) might point at the interaction between crystalline grains and the ions, it is hard to imagine that the force, which rotates the grains by 70° with an almost constant rate, depends on the crystal symmetry. A possible explanation might be the interaction between the ion beam and isotropic material in the sample. In poly-crystalline materials, the grain boundary, which is supposed to be amorphous, is a few nanometres thick. If the grains are of the size of 10–100 nm, a large part of the material is in the grain boundaries, i. e. amorphous.

Indeed, there is a well-known effect, referred to as 'ion hammering' [2, 3], which describes anisotropic dilation of amorphous materials during ion irradiation. Due to the cylindrical shape of the volume where the energy is deposited, the material is plastically lengthened in the direction normal to the ion path and shortened in the direction parallel to it. When the amorphous layer fixed on the substrate is bombarded with swift heavy ions from a direction other than normal, the dilatation is transformed into shearing of the layer away from the direction of the incoming beam.

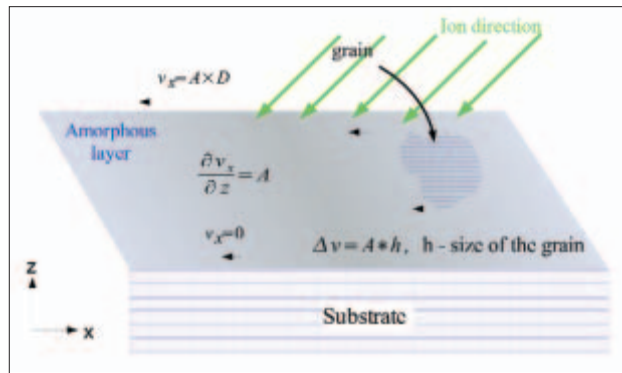


Fig. 3: Simple model for the grain rotation in amorphous matrix. Due to the geometry of the ion track, the amorphous layer is plastically sheared. A crystalline grain built into this matrix would have to rotate.

Since the grain boundary is interconnected through the whole material, we expected the nanocrystalline layer to behave like an amorphous one with crystalline grains embedded into it. As a simple model we can assume that the grain size is small compared to the distance between grains. The shearing of the amorphous layer would then produce a rotational moment on grains, and they would rotate away from the ion beam direction, as it was measured. In real nanocrystalline materials, the grains are still much larger than the grain boundary thickness, and there is an interaction between the grains. This is the reason why in some materials (e.g. α -Ti) the rotation around the surface normal takes place. Grains tend to behave like in our model, but since they are too close to each other, they jam and are not able to rotate further. They can unhook only if they rotate in other directions until the contact surfaces are parallel. Due to the energy balance, the surfaces of small grains are mostly low indexed planes, so the aligning of surfaces in grains implies also the aligning of the crystalline axes. In our measurements, this aligning is seen as breaking of the fibre texture. The actual rate of the alignment and rotation depends on the form and size of the grains.

- [1] I. Zizak, N. Darowski, G. Schumacher, S. Klau-münzer, W. Assmann, J. Gerlach, *Modification of the Ti Texture using swift heavy ions*, Hahn-Meitner-Institut Annual Report 2003
- [2] S. Klau-münzer, *Plastic flow of amorphous materials induced by swift heavy ions*, Mater. Sci. For. **97–99**, 623 (1992)
- [3] H. Trinkaus, A.I. Ryazanov, *Viscoelastic model for the plastic flow of amorphous solids under energetic ion bombardment*, J. Nucl. Mater. **246**, 244 (1997)

Corresponding author:

I. Zizak
zizak@hmi.de

Electronic energy-density effects in Auger angular distributions

G. Schiwietz¹, F. Staufienbiel¹, M. Roth¹, K. Czerski¹, P.L. Grande²

■ 1 HMI, SF4 ■ 2 Instituto de Física, Universidade Federal do Rio Grande do Sul, Porto Alegre, Brazil

In this work, we report on a new effect related to the extremely dense energy deposition of heavy ions at velocities around 10% the speed of light. In contrast to individual photons or electrons, swift heavy ions can transfer energies of several hundred eV per target atom into the electronic system of the target [1]. In fact the power deposition by a single highly charged ion is comparable to a focused multiphoton pulse of the future free electron x-ray laser XFEL that will be installed at DESY/Hamburg.

As has been shown in previous papers [1], complete ionization of all light atoms along the ion track as well as electron temperatures of about 100 000 K result from the penetration of an individual ion. Thus, locally there is extremely strong excitation accompanied by the breaking of all bonds inside a nanometer radius around the long and straight ion path. Subsequently the electronic motion is coupled to the atomic degrees of freedom (see Fig. 1) and materials modification via high-temperature or high-pressure phases may result.

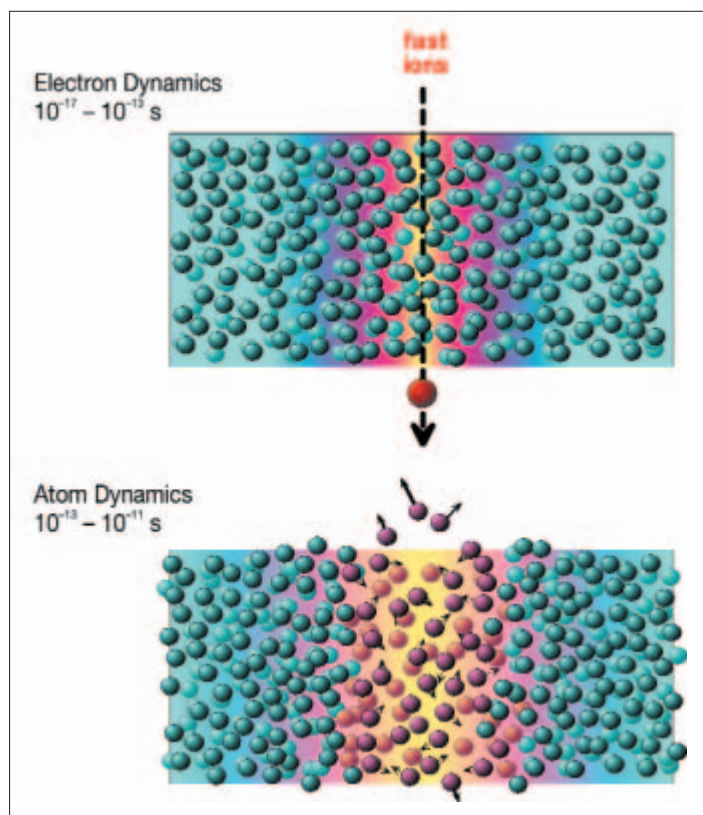


Fig. 1: Time evolution of an ion track after the penetration of a swift heavy ion (red ball with arrow). First the electronic system is heated up (color coding in the upper drawing) and afterwards the energy is transferred to the atomic system (lower drawing).

Most of the qualitative and quantitative results on electronic short time energy-density effects in ion tracks are deduced from high-resolution Auger-electron spectra corresponding to Auger-decay times of 1–10 fs. Under specific conditions inner-shell vacancies decay via (one-electron) x-ray transitions. In most cases, however, the production of Auger electrons (via two-electron transitions) is more likely. Their peak energy contains information on the ionization degree and on collective electrostatic potentials [2]. Their peak width may contain information about the populated density of states in the valence/conduction bands [3]. If a local thermal equilibrium is reached before the Auger decay, it is even possible to extract electron temperatures from the peak width. The high electron temperatures should also have an influence on the angular distribution of emitted Auger electrons, since the electron transport to the surface should be affected. The only setup at any high-energy accelerator that is sophisticated enough for such a study is the one installed at ISL (devices 1, 4, 5, and 7 in Fig. 2 are needed for this purpose).

Here we present the first angular Auger-electron distribution induced by swift heavy ions. Experiments have been performed with 592 MeV Au^{48+} ions at normal incidence on atomically clean beryllium (Be) and aluminum (Al) surfaces. For Be the so-called K^nVV Auger decay and for Al the L^nVV Auger yield as function of the emission angle has been investigated. In the latter case, a vacancy in an n -fold ionized L shell is filled by one valence electron

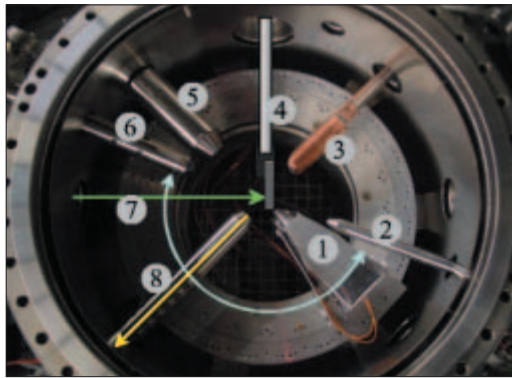


Fig. 2: Top view of the ultra-high vacuum setup with double magnetic shielding.

1) Hahn-Meitner-Institut made rotating (light blue arrows) electrostatic electron spectrometer, **2)** UV source, **3)** x-ray source, **4)** target manipulator, **5)** electron gun, **6)** low-energy Ar sputter gun, **7)** heavy-ion beam from the ISL cyclotron (green arrow), **8)** retractable (yellow arrow) secondary-ion mass-spectrometer

(**V**) and another valence electron (**V**) is being ejected. Conservation of the total electronic energy determines the Auger-electron energy. The corresponding L^iVV Auger-intensities have been measured for $n=1, 2$, and 3 . It is emphasized that such different Auger-decay channels are related to different decay times and reflect specific snapshots of the time evolution of ion tracks in solids [1]. The intensity ratios $R_2 = I(L^2VV)/I(L^1VV)$ and $R_3 = I(L^3VV)/I(L^1VV)$ (displayed as red and blue symbols in Fig. 3) will thus be sensitive to the time evolution of the ion track. Experimental uncertainties, electron diffraction or refraction effects are canceled to a large extent when calculating ratios. Previous investigations [4] have revealed cosine-like angular distributions, very similar for various targets and different types of transition. Using this information, the ratios R_2 and R_3 are expected to be constant to within a few percent.

A closer look at Fig. 3 shows that the ratios are not constant at all, with a significant minimum at ejection angles around 180° with respect to the initial beam direction (we have also observed a similar behavior for the Be target). The above discussion points to a time-dependent effect. In fact, the electron temperatures increase from about 20 000 K for L^1VV to about 50 000 K for L^3VV transitions mainly due to the mean Auger decay time which is reduced from 1.5×10^{-14} s for L^1VV to 0.5×10^{-14} s for L^3VV . Thus, the ratio R_3 is related to very high electron temperatures (50 000 K) as is estimated from the shape of the Auger line (see refs. [3]).

Furthermore, emitted electrons at angles close to 180° are moving for an extended period of time along the hot ion track. Hence, the pronounced minimum in Fig. 3 for exactly this case points to a preferential absorption of Auger electrons inside a hot electron gas. Such an effect has never been observed before. It is expected to have an influence on laser-induced plasmas as well, but it is easier to investigate this effect with spatially confined energy depositions as they are typical for ion-solid interactions.

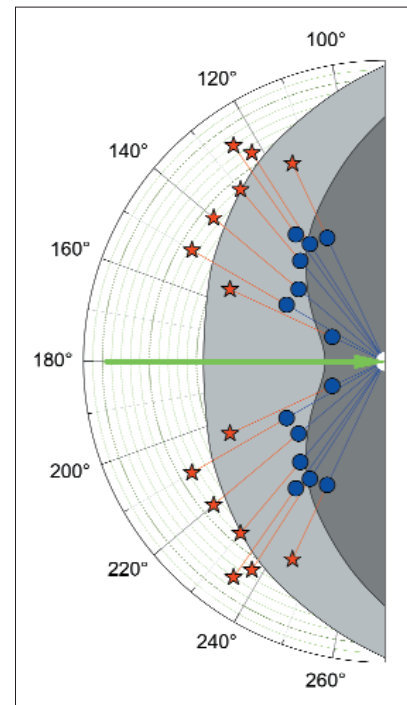


Fig. 3: Angular distribution of Auger-intensity ratios (in polar coordinates) for L^2VV to L^1VV (red asterisks) as well as for L^3VV to L^1VV (blue circles) line intensities from atomically clean Al surfaces. The green arrow indicates the incident direction of the 592 MeV Au^{48+} projectile ions.

- [1] G. Schiwietz, M. Roth, K. Czerski, F. Staufenbiel, P.L. Grande, *Femtosecond Dynamics – Snapshots of the Early Ion-Track Evolution*, Nucl. Instr. Meth. B **225**, 4–26 (2004)
- [2] G. Schiwietz, P.L. Grande, B. Skogvall, J. P. Biersack, R. Köhrbrück, K. Sommer, A. Schmoldt, P. Goppelt, I. Kádár, S. Ricz, U. Stettner, *Influence of Nuclear Track Potentials in Insulators on the Emission of Target Auger Electrons*, Phys. Rev. Lett. **69**, 628–631 (1992); G. Xiao, G. Schiwietz, P.L. Grande, N. Stolterfoht, A. Schmoldt, M. Grether, R. Köhrbrück, A. Spieler, U. Stettner, *Indications of Nuclear-Track-Guided Electrons Induced by Fast Heavy Ions in Insulators*, Phys. Rev. Lett. **79**, 1821–1824 (1997)
- [3] G. Schiwietz, G. Xiao, P.L. Grande, E. Luderer, R. Pazirandeh, U. Stettner, *Determination of the electron temperature in the thermal spike of amorphous carbon*, Europhys. Lett. **47**, 384–390 (1999); F. Staufenbiel, G. Schiwietz, K. Czerski, M. Roth, and P.L. Grande, *Electronic energy-density effects in ion tracks of metals*, Nucl. Instr. Meth. B (in print)
- [4] W.S.M. Werner, H. Tratnik, J. Brenner, H. Störi, *Surface Science* **495**, 107–119 (2001)

Corresponding author:

G. Schiwietz
schiwietz@hmi.de

Melting of orientational order of colloidal molecular crystals on a triangular lattice

A. Šarlah, T. Franosch, E. Frey

■ HMI, SF5

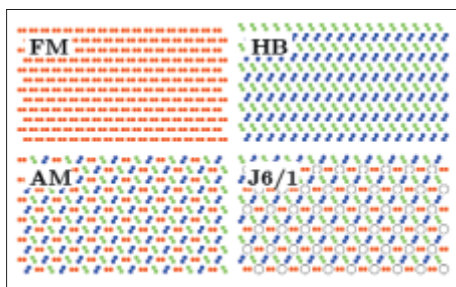


Fig. 1: Schematic representation of ordered ground states of the colloidal dimer Hamiltonian. The orientations of dimers are colour-coded. The energy of the J6/1 structure is degenerate with respect to the dimer orientation on the sites denoted by circles.

Soft condensed matter and, in particular, systems of colloidal particles can serve as versatile model systems to study phenomena of condensed matter physics. The main advantage of colloidal systems lies in the fact that the characteristic time- and length-scales allow monitoring individual particles by widely accessible methods, such as light scattering or video microscopy. Lately, research in the field of colloids has focused on two-dimensional (2D) systems, especially, on 2D colloidal systems subject to 2D periodic potentials. In experiments, the periodic patterns are mostly produced by light sources: either by arrays of laser traps or by an interference pattern of coherent laser beams. These systems are ideal to mimic the adsorption of atoms or molecules on atomic surfaces, vortices in superconductors with periodic pinning arrays, and other related phenomena studied extensively in condensed matter physics.



Fig. 2: The Japanese 6 in 1 chainmaille. Note the resemblance with the J6/1 structure of Fig. 1.

Our theoretical study has been motivated by a recent work of Brunner and Bechinger [1] who have studied the ordering and melting phenomena of 2D colloidal systems on a triangular lattice. The lattice was produced by the interference of three coherent laser beams, which allowed for a continuous variation of both the lattice constant and the strength of the laser potential. Adjusting the lattice constant and density of colloidal particles makes it possible

to realize incommensurate and commensurate situations. For now, the experimental and theoretical/computational studies [2, 3] are restricted to commensurate cases, where the number of colloidal particles is an integer multiple of the number of potential minima.

In the experiment [1], the number of colloidal particles per potential minimum was adjusted to three and the phase behaviour on increasing the strength of the external potential has been investigated. The researchers found that even at rather low light intensities the colloids tend to localize in groups of three particles at the potential minima. Upon increasing the potential strength, the number of defects, i. e., groups of two or four particles per lattice site, is observed to decrease rapidly. They become completely unobservable already for moderate intensities. Then the groups of particles on each site form nearly equilateral triangles and can be regarded as composite objects referred to as trimers. The remaining energy excitations are the orientation of the trimers with respect to the lattice direction. Due to the interaction of the trimers, long-range orientational order can be expected for sufficiently strong coupling. This can indeed be observed once the defect-free regime takes over. Interestingly, the same authors have also observed a loss of orientational long-range order at even higher laser intensities, which was interpreted as re-entrant melting.

In our study, we have derived analytically phase diagrams for commensurate systems of dimers and trimers on triangular lattices in high external fields. There, one can assume that the translational order is fully determined by the underlying lattice and the only degrees of freedom correspond to the orientations of defect-free composite objects. The analytical study has been supplemented by Monte Carlo simulations.

Our key idea is to reduce the problem to the low energy degrees of freedom by considering composite objects as being rigid. This can be done because of the separation of energy scales, i. e., the binding energy of an isolated composite object (the sum of the internal colloid-

colloid potential energy and the compression due to the external laser potential) is orders of magnitude above the thermal energy. The symmetry of the lattice and the number of constituent particles account for the shape of the composite object and its size is such that it minimizes the binding energy. The nearest-neighbour interaction lifts the otherwise degenerate orientational states, the characteristic energy scale being the thermal one. Since the colloid-colloid repulsion is typically strongly screened, the interaction between the next-nearest-neighbour composite objects can be neglected. The rising laser intensity squeezes the constituents of composite objects closer together, thus reducing the nearest-neighbour interaction. This is the mechanism driving the orientational melting at high laser intensities.

Since the triangular lattice is induced by the interference of three laser beams, the lattice sites exhibit a six-fold symmetry. This symmetry yields an effective potential, which has three minima corresponding to equivalent ground states for an isolated symmetric dimer and two for an isolated symmetric trimer. If short-time orientational fluctuations close to the potential minima are considered to be already averaged out, one is left with only a discrete set of gross orientations. Then the problem reduces to the statistical mechanics problem of a system with a finite number of discrete *spin* states at each lattice site. The characteristics of the system are hidden in the effective pair-wise interactions between *spins* in different relative orientational states.

An isolated trimer on a triangular lattice has two discrete orientational states and a pair of trimers can be in one of four configurational states, two of which are equivalent. The resulting two energy differences imply a generalization of the Ising system. However, due to the symmetry of the lattice, the problem reduces to the pure 2D Ising model, which has been solved analytically long ago. Considering this solution and determining the effective interaction energies in the sense explained above, we have determined the critical laser intensity, above which the orientational order melts. The results are in accordance with the experimental observations. It should be noted that our model has no fit parameters.

The case of dimers on a triangular lattice is much richer. A single dimer has three discrete states and a pair of dimers nine configurational states, which fall into one of four different classes. This implies a Hamiltonian with three relevant energy scales. Again, the interplay of

the symmetry of lattice and orientations of dimer states reduces the number of parameters by one, leading to a generalized 3-state Potts model. This model has four different ordered phases: ferromagnetic (FM), antiferromagnetic (AM), herringbone (HB), and Japanese 6 in 1 (J6/1), see Fig. 1. We have borrowed the name for the latter from the weaving patterns for chainmailles, see Fig. 2, worn by samurai in the 14th century. The first two ordered phases occur also in the case of a pure Potts model, though, in a certain parameter range the FM to P (paramagnetic) transition is discontinuous because it is driven by the non-Potts term. The HB structure is the one most relevant for colloidal systems. However, it is not restricted to colloidal systems. In the 1980's, a similar structure has been identified as the ground state of N₂ molecules adsorbed on graphite [4]. The theoretical description within a continuous anisotropic planar rotor model yielded critical behaviour comparable to the one obtained with our discrete analogue. At that time there was also some experimental evidence for structures having similar symmetry as our J6/1 structure. The complete phase diagram of the colloidal dimer Hamiltonian is presented in Fig. 3.

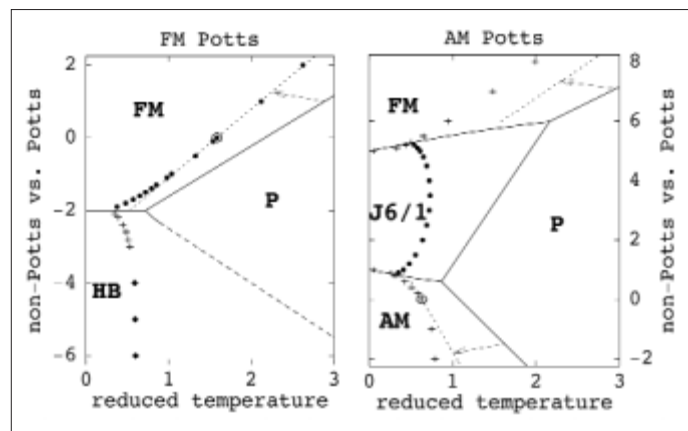


Fig. 3: Phase diagram for the dimers on a triangular lattice. The areas corresponding to structures with different symmetries (denoted by their respective names) are separated by phase boundaries obtained either within the MF description (lines) or Monte Carlo simulations (symbols).

- [1] M. Brunner, C. Bechinger, Phys. Rev. Lett. **88**, 248302 (2002)
- [2] C. Reichhardt, C.J. Olson, Phys. Rev. Lett. **88**, 248301 (2002)
- [3] A. Šarlah, T. Franosch, E. Frey, submitted to Phys. Rev. Lett. (2005)
- [4] O.G. Mouritsen, A.J. Berlinsky, Phys. Rev. Lett. **48**, 181 (1982)

Corresponding author:

A. Šarlah
andreja.sarlah@mf.uni-lj.si

Force transduction in stiff polymers

O. Hallatschek, E. Frey, K. Kroy

■ HMI, SF5

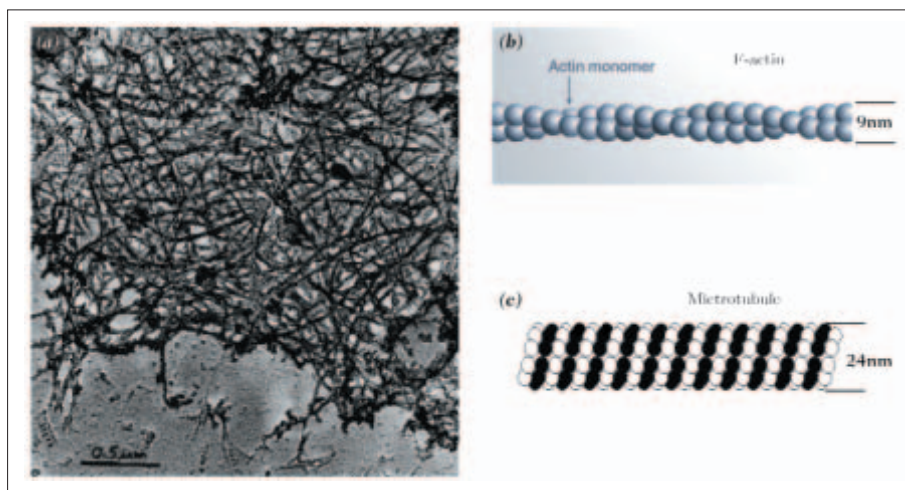


Fig. 1: In vitro networks of purified F-actin, such as the one shown in the electron micrograph **a)**, serve as model systems for studying the mechanical properties of the cytoskeleton. The cytoskeleton is a dense network mainly consisting of F-actin **b)** and microtubules **c)**. [Part **a)** courtesy of Erich Sackmann; part **b)** adapted from Ref [1]; part **c)** courtesy of Erwin Frey]

This work is motivated by the intriguing properties of a special class of biopolymers, which can be found in eukaryotic cells. It is by now well established through numerous experiments in vitro and in vivo that the extraordinary mechanical and dynamical properties of cells are to a large extent determined by a three-dimensional assembly of protein fibers, the cytoskeleton. Its structural elements are a number of relatively stiff biopolymers (actin filaments, microtubules and intermediate filaments) and proteins that crosslink them to form bundles or networks (see Fig. 1a) for a F-actin network). Microscopically, these biopolymers are linear assemblies of globular subunits. For example, actin is a twisted double-strand of beaded subunits, the globular actin, which is illustrated in Fig. 1b). It is a common feature of all cytoskeletal filaments that the molecular architecture provides them with a nearly *inextensible* backbone and a high *bending rigidity*. This is particularly evident for microtubules, which are hollow cylinders typically formed by thirteen tubulin protofilaments assembled in parallel, see Fig. 1c). As a consequence, microtubules have an enormous bending stiffness comparable to carbon nanotubes.

For the analysis of the mechanical response of biological tissues to external forces it is crucial to understand how forces (statically and dynamically) percolate through the interior of a single cell. To tackle this problem, the complexity of the cell interior may be reduced to the cytoskeleton (immersed in a viscous liquid), which is, due to its stiffness, the cell component most efficient in transmitting forces. This idealized model system exhibits complex rheological properties that can be studied in vitro. It has therefore gained considerable attention during the last decade among physicists interested in soft matter and biology.

We studied theoretically the problem of mechanical force transduction along single stiff polymers [2] – the links of a cytoskeletal network. This question arises, for example, when a stiff polymer is pulled longitudinally at the ends, see Fig. 2. In the case of an inextensible rigid rod the whole rod would be set into motion instantaneously. A thermally excited polymer, instead, will generally exhibit self-affine contour undulations and the tension has to pull these undulations (against the longitudinal friction) in order to set (a part of) the polymer into motion – just as is the case for a wiggled thread that is suddenly pulled at both ends. This stretching of the polymer occurs within a finite region close to the boundary where the force is applied.

The size $l_H(t)$ of this region increases with time until it eventually spans the entire polymer. As long as this boundary layer does not extend over the whole filament the other end will not be affected. The growth laws for the boundary layer determine how fast mechanical signals propagate through the filament.

Previous theoretical studies are mainly semi-phenomenological and give a rather incoherent picture. Markedly different growth laws have been predicted for weak [3–5] and strong [4, 6] forces, respectively. The precise meaning of “strong” and “weak” and the validity of the various assumptions in [4, 6] are not immediately obvious, such that many questions are left unanswered.

We have for the first time developed from first principles description [2, 7] of non equilibrium propagation and relaxation of the tension in stiff polymers. This theory not only recovers all cases (correctly) studied in the literature so far and identifies the range of their validity (see Fig.3). It also allows us to systematically extend these previous results and to derive the longitudinal nonlinear response to various external perturbations (such as mechanical excitations, hydrodynamic flows, electrical fields, temperature quenches etc.) that can be represented as sudden changes of ambient/boundary conditions. Due to their biological implications, we expect our results to be tested in future experiments.

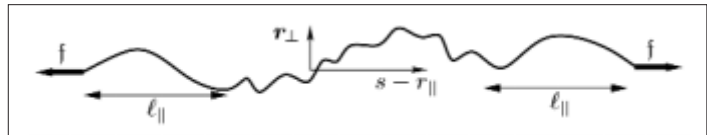


Fig. 2: Schematic illustration of a scenario involving tension propagation: In response to an external force f , the thermally undulated contour is straightened within boundary layers of growing width $l_{||}(t)$.

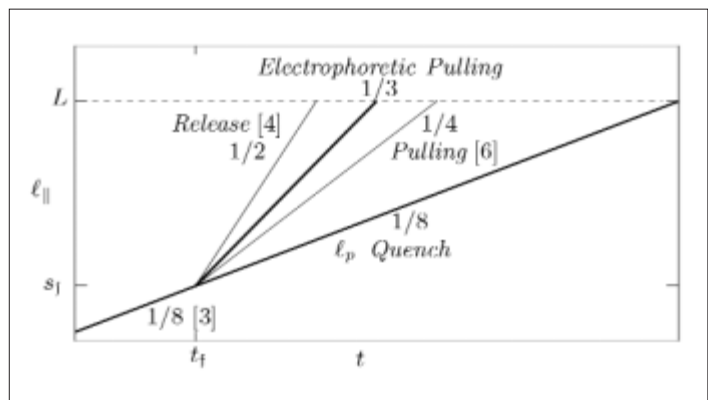


Fig. 3: Double-logarithmic sketch of the tension propagation laws $l_{||}(t) \propto t^z$. At a force dependent time t_f they cross over from a universal short-time regime to (problem-specific) tension-dominated intermediate regimes. The propagation ends when the tension has spread over the whole filament, $l_{||}(t) \approx L$.

- [1] R. Götzter, K. Kroy, E. Frey, M. Bärmann, E. Sackmann, *Macromolecules*, 29:30, (1996)
- [2] O. Hallatschek, E. Frey, K. Kroy; *Phys. Rev. Lett.* **94**, 77804 (2005)
- [3] R. Everaers *et al.*, *Phys. Rev. Lett.* **82**, 3717 (1999)
- [4] F. Brochard-Wyart, A. Buguin, P. G. de Gennes, *Europhys. Lett.* **47**, 171 (1999)
- [5] V. Shankar, M. Pasquali, D. C. Morse, *J. Rheol.* **46**, 1111 (2002)
- [6] U. Seifert, W. Wintz, P. Nelson, *Phys. Rev. Lett.* **77**, 5389 (1996)
- [7] O. Hallatschek, E. Frey, K. Kroy, *Phys. Rev. E* **70**, 031802 (2004)

Corresponding author:

O. Hallatschek
hallatschek@hmi.de

Synchrotron light helps to elucidate the role of metalloproteins in health and disease

M. Kühbacher, A. Kyriakopoulos, D. Behne

■ HMI, SF6

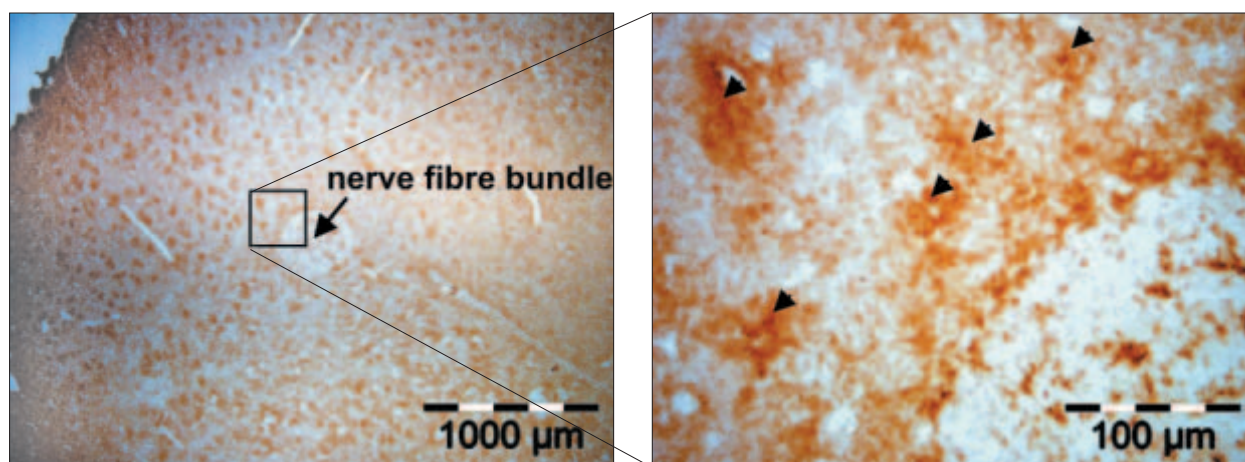


Fig. 1: Immunolabeling of the prion protein in a BSE-infected hamster brain section. The metal load of the aggregations of this metalloprotein (arrows) can be investigated by SRXRF.

Most of the metals and metalloids present in the mammalian organisms are bound to proteins. These metalloproteins play a central role as structural or catalytic components, and their identification and the elucidation of their distribution and biological functions are therefore of great interest in various fields of the life sciences. Synchrotron radiation X-ray fluorescence analysis (SRXRF) allows the determination of the metal distribution in cryosections of tissues while synchrotron radiation-based Fourier transform infrared (SRFTIR) spectromicroscopy may provide information on the chemical composition of the sections of interest. These methods can therefore be used as valuable tools in studies on the role of metalloproteins in health and disease. Their application in this field of research is subject of our work at the IRIS Beamline at BESSY and the SRXRF beamline of HASYLAB. In both cases the use of synchrotron radiation offers the high spatial resolution necessary in the investigation of thin tissue sections.

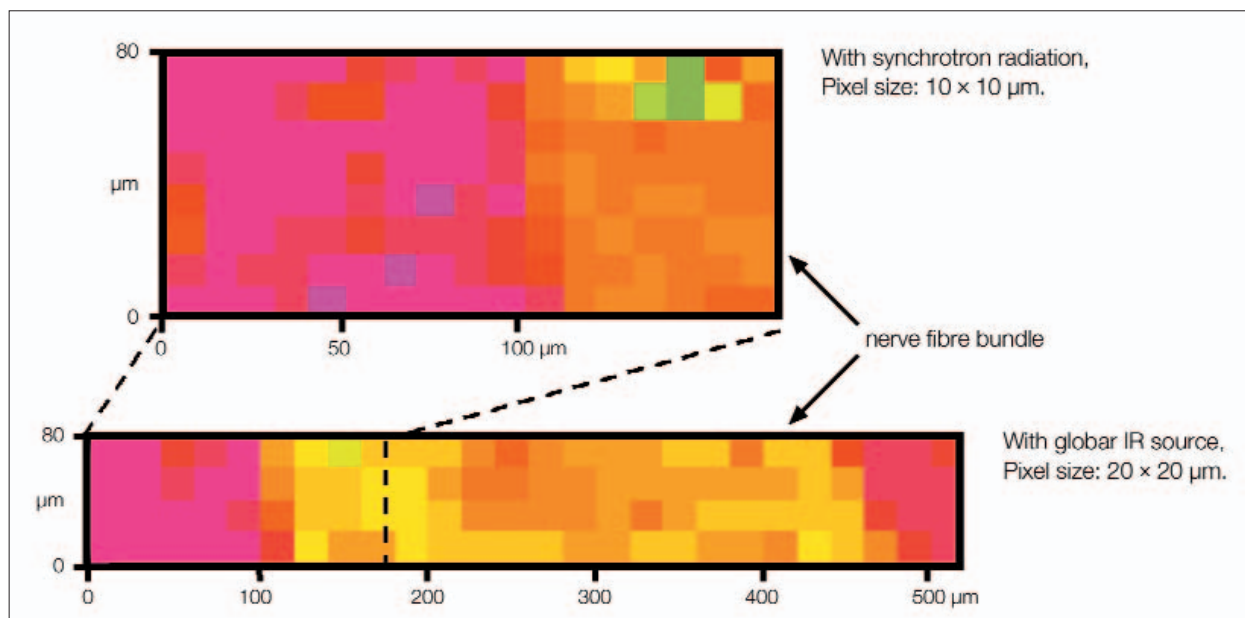


Fig. 2: Colour-coded lipid-to-protein ratio determined by SRFTIR-spectro-microscopy in a hamster brain section with a lipid-rich nerve fibre bundle as shown in Fig. 1. The example illustrates the higher spatial resolution achieved by synchrotron as compared with that obtained by a global IR source.

There is evidence that metals and metalloids such as copper, manganese, zinc and selenium are involved in the etiology of Transmissible Spongiform Encephalopathies (TSEs). TSEs such as Scrapie in sheep, Bovine Spongiform Encephalopathy (BSE) in cattle, or Creutzfeldt-Jakob disease in man are infectious neurodegenerative disorders of the central nervous system. TSEs are associated with the conformational change and the aggregation of a specific protein. This *prion protein*, found in nerve and glial cells throughout the brain, was shown to bind copper, zinc, and manganese, and changes in the binding of these metals may play a role in the pathogenesis of TSEs. Our studies on the role of metalloproteins in these diseases therefore include investigations of changes in the elemental distribution in the brain carried out by SRXRF as well as the measurement of structural changes of specific proteins by means of SRFTIR-spectro-microscopy at the IRIS-Beamline at BESSY.

The localization of metal-containing proteins in histological tissue sections was achieved at the SRXRF beamline of HASYLAB by means of a capillary optical device focusing the X-ray beam with a spatial resolution of $15\ \mu\text{m}$. Brain samples were obtained from hamsters which had been infected with different TSE strains. The tissue samples were provided by M. Beekes and A. Thomzig from the Robert-Koch-Institut, Berlin. The measurements included the determination of the distribution of phosphorus, sulfur, chlorine, potassium, calcium, iron, copper and zinc and the immuno-histochemical detection of the prion protein. The most important finding so far was the detection of unusual copper hot-spots with a mean diameter of about $30\ \mu\text{m}$ which were found in the brain sections of all hamsters infected with TSE.

Corresponding author:
M. Kühbacher
kuehbacher@hmi.de

25 years of the magnetic spectrometer Q3D

H. G. Bohlen, W. von Oertzen

■ HMI, SF7

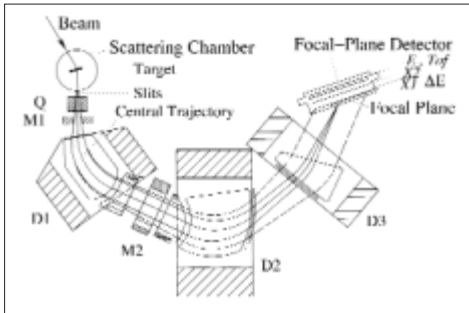


Fig. 1: Magnetic Spectrometer Q3D

Magnetic spectrometers for the measurement of high resolution energy spectra of charged particles are among the most powerful instruments in nuclear physics and other fields of heavy ion research. Q3D spectrometers consisting of a quadrupole Q, three dipoles (D1–D3) and other magnetic multipole elements (M1, M2) (see Fig. 1) combine a large solid angle with the best resolution in the range down to $\delta E/E \approx 2 \times 10^{-4}$. The spectrometer Q3D at the ISL accelerator facility of the Hahn-Meitner-Institut has now been in operation for 25 years. In combination with the high quality ion beams from the ISL cyclotron and with modern detector technology in the focal plane including advanced data acquisition systems, it offers unique possibilities for reaction studies in the energy range of 5–30 MeV/u. In the past years 19 Diploma and 15 PhD theses (100 publications) have been accomplished at this instrument [1].

We give here a short description of the spectrometer and an overview of the main physics subjects in this period. The layout of the magnetic elements is depicted in Fig. 1. The quadrupole Q produces a vertical cross at M2 in order to increase the vertical angular acceptance ($\pm 3^\circ$). All the focusing in the horizontal plane is achieved by the boundaries of the dipoles. The kinematical momentum variation within the horizontal angular acceptance of $\pm 3^\circ$ is corrected by the multipole M2 using the variable quadrupole component. The detector system in the focal plane allows measuring the position of ions (needed for the momentum analysis of the reaction products), their energy loss, their rest energy and the flight-time, which depends on the path through the spectrometer. The latter dependence also allows one to determine the scattering angle for identified isotopes with a resolution of 0.3° . For example, in the rainbow scattering of $^{16}\text{O} + ^{16}\text{O}$ (Fig.3) pieces of angular distributions with a width of 10° in the centre of mass were measured with this resolution. In other cases,

the difference in the angular variation of kinematical lines observed for different target masses can be used to separate reactions on contaminants in the target (typically ^{12}C and ^{16}O). The examples given below show the potential for experiments with heavy ions.

Measurement of spin alignment using the Doppler-Effect in particle spectra

An example of the high resolution capability of the spectrometer is the measurement of the energy shifts $\Delta E = \pm(v/c) \times E_\gamma$ of reaction products with γ -decay in flight (v speed of the ion, E_γ decay energy). The angular distribution of the γ -rays, which depends on the spin alignment and

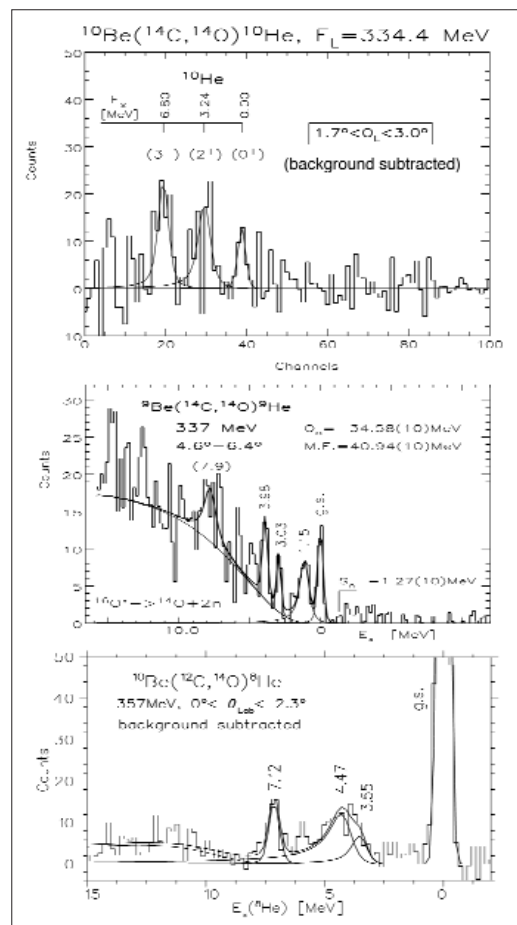


Fig. 2: Spectra of the extremely neutron-rich helium isotopes ^{10}He (upper panel), ^9He (centre panel) and ^8He (lower panel)

on the multi-polarity of the γ -transition, is reflected in a specific shape of the broadened energy distribution. The latter is used to deduce the spin alignment, which is a very important parameter in the understanding of nuclear reactions [2].

Measurements of ground state masses and energy spectra of very exotic nuclei

The Q3D spectrometer allows the measurement of reaction products in multi-nucleon transfer reactions with very small cross sections. In addition it is possible, with a corresponding calibration, to determine the mass of exotic nuclei and their excited states, which may be particle-stable or unstable. Also the measured decay width can be analyzed, which allows to deduce spectroscopic information on the orbital angular momentum and the spin of the states. An example of these studies is the determination of the level structure of the helium isotopes ^8He , ^9He and ^{10}He as shown in Fig. 2. The mass of ^{10}He , which has the largest neutron-to-proton ratio of all known nuclei, was determined [3] and several excited states of the three isotopes have been measured [3, 4]. The ^{10}He ground state resonance has a measured width of only 0.3(2) MeV. This can be understood from the fact that a direct decay of $^{10}\text{He} \rightarrow (n + ^9\text{He})$ is not possible, and the three particle channel $(n + n + ^8\text{He})$ with a much more restricted phase space is the only direct decay mode. Similarly, the energy levels of the highly exotic isotopes ^{10}Li and ^{11}Li have been measured [4]. For both nuclei, ^{11}Li and ^{10}He , the binding is achieved by a special quantum mechanical structure of the three body systems $(n + n + ^9\text{Li})$ and $(n + n + ^8\text{He})$. The wave functions of the neutrons have a very large extension beyond the range of nuclear forces, a phenomenon referred to as "Halo"-structure. Another highly appreciated subject, which has been the domain of Q3D experiments, is the establishment of covalently bound nuclear two- and three-centre systems. These are nuclear dimers in Be-isotopes and nuclear polymers as linear chains in excited states of ^{13}C and ^{14}C nuclei [5]. Examples of these unique results are given in the next contribution.

Nuclear rainbow scattering

The enhancement of cross sections at large scattering angles, which can occur for refractive scattering due to the *rainbow effect*, has been demonstrated for the first time for heavy ions with measurements at the Q3D spectrometer of the Hahn-Meitner-Institut [6]. The rainbow scattering produces an intensity maximum at the *rainbow angle*. The structure is described by Airy-functions. After the discovery [6] of this effect in the $^{16}\text{O} + ^{16}\text{O}$ system at an incident ener-

gy of $E_L = 350$ MeV, the group at the Hahn-Meitner-Institut has pursued a programme to measure the energy systematics [7] (the highest energies at the spectrometer SPEG at GANIL). Figure 3 shows the evolution of the refractive rainbow structure as function of energy, here expressed by the de-Broglie wavelength of the ^{16}O particles. The effect can be expressed by a refractive index, which is determined by the strongly attractive nucleus-nucleus potential.

Energy loss of ions in extremely thin layers

The energy loss of ions in matter is well understood in charge-state equilibrium conditions, i. e. in thick materials. However, for high resolution elastic recoil detection analysis (ERDA), where thicknesses range down to a few nanometres, the analysis relies on calculations of the energy loss of the incoming ion. With the method developed at the Hahn-Meitner Institute [8] the whole matrix of values for energy losses in very thin carbon foils in dependence on both the incoming and the outgoing charge states has been obtained for ^{18}O , ^{22}Ne and ^{40}Ar ions [8]. These values will also serve to calibrate the calculations of energy losses of ions penetrating hot and dense plasmas.

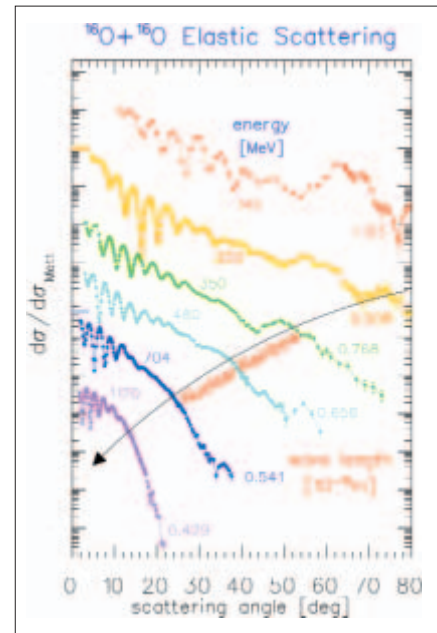


Fig. 3: Data of elastic scattering of $^{16}\text{O} + ^{16}\text{O}$ at different incident energies as indicated at the data. The effect of nuclear rainbow scattering is observed at large scattering angles.

- [1] <http://www.hmi.de/bereiche/SF/SF7/q3d.html>
- [2] H. G. Bohlen, *et al.*, Z. Phys. A **285**, 371 (1978)
- [3] A. N. Ostrowski, *et al.*, Phys. Lett. B **338**, 13 (1994)
- [4] H. G. Bohlen, *et al.*, Nucl. Phys A **583**, 775 (1995)
- [5] W. von Oertzen, *et al.*, Eur. Phys. J. A **21**, 193 (2004)
- [6] E. Stiliaris, *et al.*, Phys. Lett. B **223**, 291 (1989)
- [7] D. T. Khoa, *et al.*, Nucl. Phys. A **672**, 387 (2000)
- [8] A. Blazevic, *et al.*, NIM B **190**, 64 (2002)

Corresponding author:

H. G. Bohlen
bohlen@hmi.de

Chain states in ^{13}C and ^{14}C , nuclear polymers

W. von Oertzen, H. G. Bohlen

■ HMI, SF7

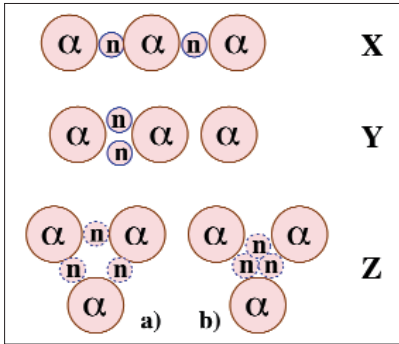


Fig. 1: Molecular configurations in ^{14}C : three α -particles with valence neutrons. Linear chains with different sharing of the neutrons: **X)** the symmetric configuration; **Y)** intrinsically reflection-asymmetric. Oblate shapes (**Z**) with two ways of sharing the valence particles.

Recent studies [1–2] of excited states in light nuclei show that the binding between clusters due to the exchange of valence neutrons results in covalently bound molecules. We have studied the cluster structure of beryllium isotopes ^9Be – ^{12}Be and more recently we have identified the molecular cluster structure of excited states in ^{13}C and ^{14}C . Inspecting the available data compilations and using the selectivity of various multi-nucleon transfer reactions, we apply the concept of *complete spectroscopy* and identify the states with single particle structure, and those states with clustering, the latter are expected to form rotational bands. These cluster states in ^{13}C and ^{14}C consist of three α -particles and are stabilised by the covalent valence neutrons. Chain states with very large deformation (hyper-deformation) are identified. Due to their intrinsically reflection asymmetric shapes the rotational bands are observed as parity (inversion) doublets, as described by Herzberg [4] for atomic molecules. After a detailed study of dimers, the covalently bound states of two α -particles [1–3] in the beryllium isotopes, the covalent bond between three α -particles can be modelled with the Hueckel-method for three centres as described for ^{13}C in ref. [5]. In the nuclear case the three centre system can have different geometrical arrangements. In ^{14}C for example the different cluster configurations to be expected are:

- a) Linear reflection-symmetric chains corresponding to a configuration with the valence particles equally distributed among the three basis centres (α -n- α -n- α), labelled as the *X-configuration* in Fig.1. For the valence particles of the lowest chain state, the $K=3/2$ band with orbitals build from the π -bonds between two α -particles, the density distri-

butions will be concentrated outside the symmetry axis. The most stable isomeric nuclear three centre molecule is expected to be observed in ^{16}C , with the linear structure chain (α -2n- α -2n- α), the study of such states is the aim of our future investigations.

- b) Linear intrinsically reflection *asymmetric* configurations corresponding to the structure α -2n- α - α with the two valence neutrons in the covalent π -bond between two centres. In this case with a α -2n- α substructure as in ^{10}Be (g.s.), which has a large pairing energy, we obtain the *Y-configuration* in Fig.1. Therefore close to the threshold for ($^{10}\text{Be} + \alpha$) at 12.012 MeV we expect two rotational bands as parity inversion doublet [6] of this structure.
- c) The oblate configurations will be represented by a triangular structure (also shown in Fig.1) as discussed in refs. [5, 6]. In this case the π -bonds would penetrate the α -particles and it is expected that the σ -bonds dominate.

In the approach of complete spectroscopy applied to ^{13}C we had previously singled out those states for which strong evidence for α -cluster structure is available [5]. These states are shown in a diagram in Fig.2, and the states can be grouped into two rotational bands with $K=3/2$, a parity doublet as expected for an asymmetric linear chain, the bands start close to the ($^9\text{Be} + \alpha$)-threshold.

Rotat. bands, K^π	$\hbar^2/2\theta$ (keV)	Configuration
^{13}C , $3/2^-_2, 3/2^+_3$	190	chain {5}
^{14}C , $0^+_2, 3^-_2$	230, 280	oblate {6}
^{14}C , $0^+_3, 1^-_2$	120, 130	chain {6}

Table 1: Properties of the rotational bands of ^{13}C and ^{14}C with 3α -chain or triangle (oblate) configurations. The bands are characterized by the spin-parity K^π of the band head. Moments of inertia are given as $\hbar^2/2\theta$.

Oblate and prolate chain states in ^{14}C

We have recently successfully identified the chain states in ^{14}C as the next important step in the establishment of the structure of nuclear polymers [6]. In order to identify the cluster states in ^{14}C , using the concept of *complete spectroscopy* as in the case of ^{13}C [5], we have first identified the single particle and two-neutron-configurations in ^{14}C .

The structure of the remaining states with cluster configuration is characterized by their different population through the selectivity in many different multi-nucleon transfer reactions studied with 3D-Spectrometers. In some of these reactions states with multi-particle multi-hole configurations, involving in particular also proton excitations, become dominant. The states, which are identified as cluster states are strongly deformed, they form rotational bands with extreme deformations. Some of these states, as mentioned before, will have intrinsically reflection-asymmetric shapes. The parity projection produces in this case two bands and these are grouped into parity doublets with band-heads below the energies of the relevant thresholds corresponding to asymptotically asymmetric fragmentations.

We summarize the result for the strongly deformed cluster bands in $^{13-14}\text{C}$ in Fig. 3, by plotting the excitation energies of the states as function of $J(J+1)$, where J is the angular momentum. We notice that the slope parameter $\hbar^2/2\theta$ for the prolate ^{14}C chain states are smaller (due to larger moments of inertia) than for ^{13}C .

From these data on the rotational bands we can derive moments of inertia θ , expressed by the volume of $\hbar^2/2\theta$ listed in Table 1, and we can compare these values with those obtained for strongly deformed cluster bands in other light systems. From this result we can deduce, that the bands identified as chain states in the carbon isotopes are indeed cases of linear chain states.

Work in part supported by the German Federal Ministry of Education and Research under contract Nr. 06-OB-900.

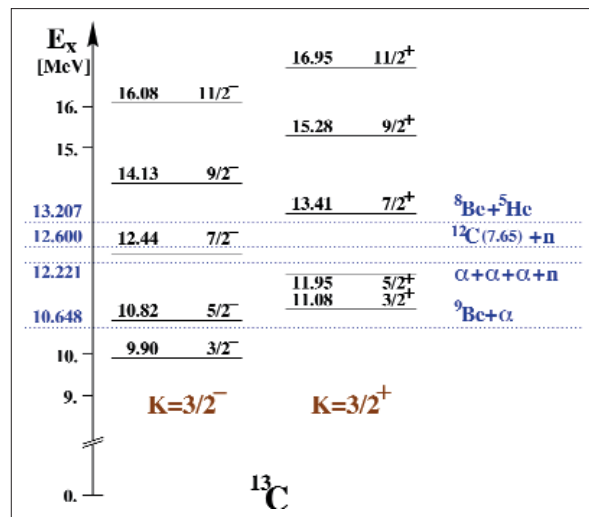


Fig. 2: Energy levels of ^{13}C grouped into rotational bands (parity doublets), the K -quantum numbers is indicated. The threshold energies for structure components related to the asymptotic cluster-structure of states are shown (from ref. [5]).

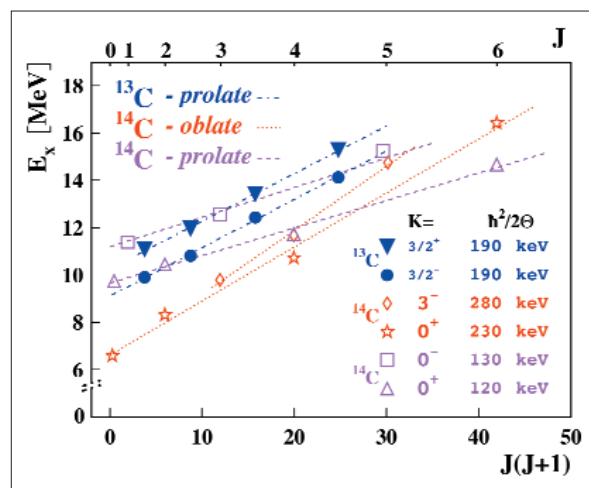


Fig. 3: Summary of strongly deformed cluster bands in $^{13-14}\text{C}$. Excitation energies are shown as function of $J(J+1)$, K -quantum numbers of the different bands are indicated. The moments of inertia expressed as $(\hbar^2/2\theta)$ indicate that the states are extremely deformed ("hyperdeformation").

1. W. von Oertzen, Prog. Theor. Physics (Japan), Suppl. No **146**, 169 (2002)
2. H. G. Bohlen *et al.*, Prog. Part. Nucl. Phys. **42**, 17 (1999)
3. W. von Oertzen, H. G. Bohlen, C. R. Physique **4**, 465 (2003)

4. G. Herzberg, *Spectra of Diatomic Molecules*, van Nostrand, Inc., Princeton (1964)
5. M. Milin, W. von Oertzen, Eur. Phys. J. A **14**, 295 (2002)
6. W. von Oertzen, H. G. Bohlen, M. Milin *et al.*, Eur. Phys. J. A **21**, 193 (2004)

Corresponding author:

W. von Oertzen
oertzen@hmi.de